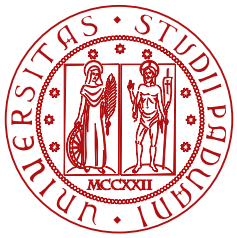

Università degli Studi di Padova

Dipartimento di Fisica e Astronomia Galileo Galilei

Department of Physics and Astronomy

Bachelor's Degree in Astronomy

Characterization of a Deformable Mirror for astronomical applications

Candidate

Nicholas Friso

Student ID 1125451

Supervisor

Prof. Roberto Ragazzoni

Co-supervisor

Dott. Gabriele Umbriaco

Dott. Alessandro Ballone

Academic Year 2022/2023

Date 14/12/2023

All WE have to decide is what to do with the time that is given us.

List of acronyms

AO Adaptive Optics

BE Beam Expander

DM Deformable Mirror

EFL Effective Focal Length

FOV Field Of View

INAF Istituto Nazionale AstroFisica

LGS Laser Guide Star

MCAO Multi Conjugate Adaptive Optics

MOAO Multi Object Adaptive Optics

NGS Natural Guide Star

OAPd Osservatorio Astronomico di Padova

PBS Pellicular Beam Splitter

PDU Power Distribution Unit

PLICO Python Laboratory Instrumentation COntrol

PSF Point Spread Function

RMS Root Mean Square

RTC Real Time Controller

SCAO Single Conjugate Adaptive Optics

WFS WaveFront Sensor

XAO eXtreme Adaptive Optics

Abstract

In this thesis, I will present the characterization of a deformable mirror. Through the description of adaptive optics, I will demonstrate the compensation of a perturbed wavefront. This also involves an exploration of the modal framework and the decomposition of a wavefront using Zernike polynomials. The setup of a testing bench for the deformable mirror will be detailed, encompassing the construction, alignment, and stability testing of the optical system. Additionally, I will cover the creation of an influence function, the creation of the best flat surface of the mirror, and the analysis of the deformable mirror actuator response. Throughout these processes, Zernike coefficients will be analyzed using interference images acquired by a professional Twyman-Green interferometer.

Sommario esteso

Nel corso della storia, l'umanità è sempre stata affascinata dal cosmo e, per millenni, l'occhio fu lo stumento usato per esplorare l'universo. A partire dal 1608, però, tutto cambiò tramite l'invenzione di Lippershey del telescopio e le migliorie apportate da Galilei. Le scoperte dei crateri lunari, degli anelli di Saturno e delle lune gioviane furono solo l'inizio.

A diffrenza del passato, dove i limiti osservativi erano dettati dagli strumenti utilizzati, l'avvento di tecnologie sempre più moderne hanno portato l'atmosfera a divenire la formidabile barriera che, oggi, ostacola lo studio dei misteri contenuti nell'universo.

Sia l'opacità dell'atmosfera a differenti lunghezze d'onda o la presenza di turbolenza in atmosfera, l'astronomia ha seguito due strade: la prima ha condotto alla difficile e costosa costruzione di telescopi spaziali mentre la seconda ha portato miglioramenti ai telescopi terrestri attraverso tecnologie immaginate negli anni '50 ed applicate nell'ambito astronomico solo negli anni '90. In questa tesi si approfondirà il secondo percorso.

Partendo dal capitolo 2, grazie ai lavori di Max [1], Hardy [2] e Madec [3], si è introdotta la nozione di risoluzione di un telescopio e deterioramento di questa dovuto principalmente al concetto di turbolenza e seeing atmosferico: il parametro di Fried, il tempo di coerenza, il rapporto di Strehl e l'angolo isoplanatico hanno aiutato in questa descrizione. Per capire come i telescopi riescono comunque ad operare in condizioni prossime al limite di diffrazione, si è descritta l'ottica adattiva e i sotto sistemi che la compongono, come rilevamento e correzione di fronte d'onda e processamento dati; come si capirà, un elemento fondamentale dell'ottica adattiva sono gli specchi deformabili ed è per questo che si sono introdotte alcune tecnologie e specifiche tecniche che li caratterizzano. Inoltre si è presentato un esempio di "loop" chiuso e alcune applicazioni scientifiche come SCAO, MCAO, MOAO e XAO.

Nel capitolo 3, utilizzando i lavori di Krishna and Dasari [4] e Ragazzoni [5] (contenuto nella lista delle pubblicazioni riguardanti il Telescopio Nazionale Galileo[6]), si è dovuto introdurre il concetto matematico di scomposizione di fronte d'onda applicata nell'ottica adattiva: si è presentata la descrizione matematica della base polinomiale ortogonale di Zernike con la rappresentazione in indici di Noll. Alla fine di questo capitolo sono stati forniti i primi 17 modi di Zernike, utilizzati in questa tesi e durante il lavoro in laboratorio, presentando la loro forma polinomiale e il corrispondente fronte d'onda.

Nel capitolo 4, si sono descritte le operazioni necessarie all'assemblaggio di un banco ottico utili alla caratterizzazione di uno specchio deformabile che, a breve, verrà utilizzato

da INAF OAPd per testare un sistema di ottica adattiva. Dopo una presentazione sui vari componenti utilizzati, come lo specchio deformabile ALPAO DM292, un interferometro professionale Twyman-Green e un beam expander, sono state esaminate due configurazioni diverse dovute dalla presenza, costruzione e instabilità del beam expander. Dopo l'introduzione del primo disegno ottico e assemblaggio, che hanno fatto emergere problemi riguardanti le aberrazioni introdotte, si è riportata la seconda configurazione, nella quale si sono osservati problemi di instabilità dovuti all'espansione termica dei telai su cui erano montate le lenti. La costante varazione dei coefficienti di aberrazioni introdotte dalle ottiche è ciò che ha portato al fallimento di alcuni test riportati successivamente.

Il capitolo 5 inizia con la discussione riguardante i tre test utili alla caratterizzazione dello specchio deformabile: il calcolo della influence function, la ricerca della miglior forma piatta, risultata avere un RMS di 31.6 nm corrispondente ad una accuratezza $\lambda/20$, o il suo miglioramento a $\lambda/43$ utilizzando un secondo interferometro, e lo studio della risposta degli attuatori dello specchio, di cui ho verificato la linearità. La tesi si conclude con una dimostrazione pratica delle funzionalità dello specchio deformabile utilizzato, al fine di provare come questo possa essere usato nell'ambito dell'ottica adattiva per correggere fronti d'onda distorti. In un primo test, si sono applicate ed osservate le prime 17 aberrazioni attraverso il fronte d'onda ricevuto dallo specchio e la relativa PSF catturata da una camera CMOS, presente in un secondo cammino ottico. In un altro test, le più comuni aberrazioni, tipiche di vere osservazioni al telescopio, sono state applicate con una determinata ampiezza tale da simulare la perdita di risoluzione in un sistema binario.

Contents

1

Introduction

Throughout history, humanity has always been fascinated by the cosmos and, for millennia, the naked eye was the tool to explore the universe. But, after 1608, everything changed with the invention of the telescope made by Lippershey and its improvements made by Galilei. The discoveries of the craters of our moon, the rings of Saturn and Jupiter's moons were just the beginnings.

While once the limitations of the observation were due to the instruments used, the technology evolved until the atmosphere itself, which envelops and protects our planet, became the formidable barrier that nowadays obstructs the mysteries of the universe.

Whether it be the opacity of the atmosphere at different wavelengths or the presence of turbulence in it, the humankind followed two paths: one landed us with in-orbit telescopes which are quite difficult and expensive to build, the other brought us improvements on ground-based telescopes made by technologies envisioned in the 1950s and applied in astronomy in the 1990s. In this thesis, I am going to delve into the second route.

In Ch. 2, following the works of Max [1], Hardy [2] and Madec [3], I will introduce the notion of telescope resolution and its deterioration due to the concept of atmospheric turbulence and seeing; I will describe how adaptive optics is used in trying to make the telescope reach its diffraction limit through wavefront sensing, wavefront correction, and data processing; I am also going to talk about deformable mirrors, their characteristics, and how they are controlled in the so-called "closed loop". I will finish by mentioning some applications of adaptive optics in astronomy.

In Ch. 3, the works of Krishna and Dasari [4] and Ragazzoni [5][1] are used to introduce the concept of wavefront decomposition applied by adaptive optics; in particular, I am going to present the orthogonal polynomial base of Zernike, its mathematical de-

[1] Part of the Telescopio Nazionale Galileo publication listed by Boschin [6]

scription and its representation in Noll's indices. This chapter will finish by showing the first 17 Zernike modes used in later chapters, their polynomial characterization and the corresponding wavefront.

As will be clear from Ch. 2, deformable mirrors are a key component in adaptive optics. That is why, in Ch. 4, I am going to describe the process I followed to set up an optical bench with the intention of characterizing one which, in the near future, will be used by Istituto Nazionale AstroFisica (INAF) - Osservatorio Astronomico di Padova (OAPd) for testing an adaptive optics system. I will go through the instrumentation used, like the deformable mirror itself, a professional Twyman-Green interferometer and a beam expander; I will discuss two different setups which emerged, mainly due to the presence of the beam expander, its construction and instability, which will also be analyzed in detail. Optical designs and assembly description will be presented.

In Ch. 5, I will detail the 3 steps I took to characterize the deformable mirror: the creation of the influence function, a matrix used to control the mirror; the finding of the best possible flat shape of the mirror; the study of the linear response of the mirror actuators. At the end of this chapter, I am going to demonstrate some capabilities of the deformable mirror starting from showing the first 17 aberrations as the wavefront coming from the mirror and their corresponding point spread function, and finishing with the loss of resolution in simulated binary systems affected by the most common aberrations, found during observations, that were set through the deformable mirror. This proved that the tested deformable mirror could be used in adaptive optics to correct a disturbed wavefront.

2

Adaptive optics compensation

This chapter is constructed around the works of Max [1], Hardy [2] and Madec [3].

The angular resolution of a telescope can be characterized by the Rayleigh criterion that defines the minimum angular separation between two point sources that can be resolved: in a perfect world, using a diffraction limited system, this resolution can be calculated as the angle between the center maximum and the first minimum of the interference pattern, the so-called Airy disk or Airy pattern[7] (in the case of a circular aperture) (Fig. 2.1a), that is created in the focal plane of the system. This can be approximated as

$$\theta \approx 1.22\frac{\lambda}{D}, \tag{2.1}$$

where λ is the observation wavelength and D the diameter of the entrance pupil of the telescope. As it can be seen from Eq. 2.1, the angular resolution can be improved by increasing the diameter of the primary mirror of a telescope.

In the case of ground-based telescopes, the "ideal" resolution described above deteriorates due to different reasons:

- the optical design, manufacture and construction, which introduce deviations from the perfect and ideal system, for example the introduction of astigmatism and coma in large field of view telescopes or the mirror deformations caused by its own mass;
- the presence of the atmospheric turbulence, the one that causes the highest degradation;
- the weathering of the surfaces by age, humidity or dust.

The latter will not be discussed in this thesis.

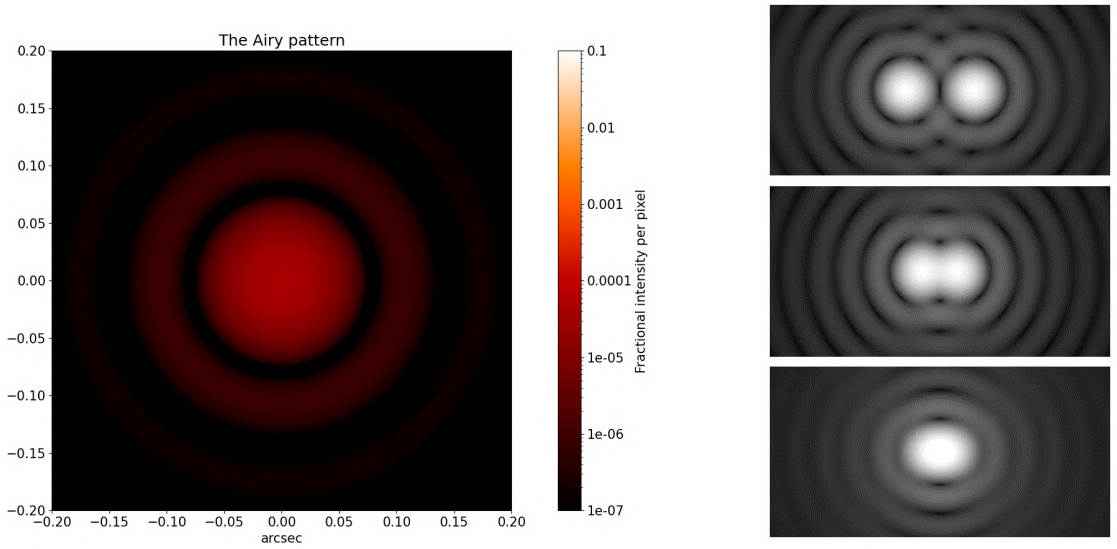

(a) (b)

Figure 2.1: On the left, a simulated Airy pattern (1 m entrance pupil at 632.8 nm) and, on the right, an example of loss of resolution according to the Rayleigh criterion (credit https://www.e-education.psu.edu/mcl-optpro/book/export/html/803 as of Nov. 2023.)

The problems introduced by the first point are usually solved by engineering optimal designs and frames and also by using correcting lenses or deformable mirrors through the so-called "active optics" system.

When it comes to the atmosphere, with its chaotic behavior between layers of air that negatively influence the straight propagation of light rays, one can distinguish two zones: the boundary layers, right above the surface of the Earth, which are characterized by the turbulence created, for example, by the heat transfer from the surface of the planet, the electronics in the dome or the telescope itself; and the "free atmosphere", just above these layers, where the turbulence is strong in frequently-discrete layers until it reaches a local maximum at the tropopause (height of 10-15km) due to the presence of a large number of wind shear (Fig. 2.2). These two regions are responsible for different wavefront distortions where the boundary layers mostly create the so-called low-order aberrations, while the "free atmosphere" also adds high-order ones.

The turbulence, which creates local variations of pressure and temperature, can be described by the Kolmogorov theory [8] that predicts its spectrum in the case that it is fully developed in the stationary and inertial regime. This theory also shows how fluctuations of the local refraction index n are proportional to the kinetic energy of the turbulence vortexes and, consequently, to their dimension.

The effects of the variation of atmospheric pressure P and temperature T on the light that passes through turbulence, regarding the local refraction index n or its deviation

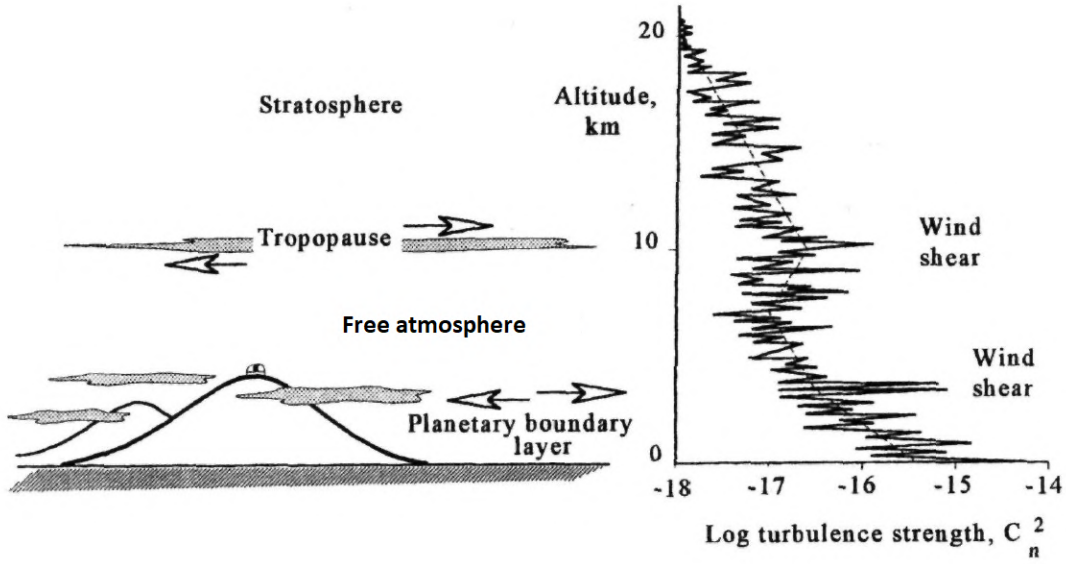

Figure 2.2: Atmosphere structure and typical turbulence profile (credit Hardy [2])

from the unity N, are encapsulated by the Cauchy's equation

$$N \equiv n - 1 = \frac{77.6 \times 10^{-6}}{T}\left(1 + \frac{7.52 \times 10^{-3}}{\lambda^2}\right) \times \left(P + 4810\frac{\varrho}{T}\right), \tag{2.2}$$

where λ is the observing wavelength and ϱ the vapor pressure of water. The resulting fluctuations of the index of refraction cause distortion and degradation of the flat wavefront entering the atmosphere: this effect is also known as atmospheric seeing.

The seeing can be described by some parameters:

- the one that represents the distance over which the wavefront phase stays correlated is called Fried parameter or atmosphere coherence length r_0; it shows the separation between two points on the telescope primary mirror where the wavefront phase correlation has fallen by $1/e$; r_0 has a dependency on the turbulence strength $C_N^2(z)$ (z being the height) and wavelength of observation λ

$$r_0 \propto \lambda^{6/5}\left[\int_0^\infty C_N^2(z)\,dz\right]^{-3/5}; \tag{2.3}$$

- the coherence time τ_0 is the timescale over which a sub-aperture of the telescope sees a coherent wavefront; this takes into consideration the wind speed V_w which causes the movement of the air masses and contributes to the constant variation of r_0

$$\tau_0 \propto \frac{r_0}{V_w}; \tag{2.4}$$

- the Strehl ratio is the ratio between the peak intensity of the observed Point Spread Function (PSF) and the ideal diffraction limited PSF;

- the isoplanatic angle θ_0 is the angle over which the wavefront degradation is well correlated; the turbulence creates decorrelations as the field of view increases since it spreads along the light path; this entails the relation between isoplanatic angle and turbulence distance h from the telescope

$$\theta_0 \propto \frac{r_0}{h}. \tag{2.5}$$

To remove atmospheric seeing while also getting the telescope resolution close to its diffraction limit, achieving an enhanced angular resolution and an increase in the peak intensity of the PSF, Adaptive Optics (AO) are implemented.

AO usually consists of a system or module in a telescope that allows us to precisely correct a perturbed wavefront through a feedback-loop procedure with the objective of reaching the unity in regards to the Strehl ratio. This is accomplished through three main subsystems that communicate with each other: wavefront sensing, wavefront correction, and data processing.

The function of wavefront sensing is to measure the deviations of a wavefront from its original flat shape all across the entrance pupil of the telescope; usually, this is done by measuring the wavefront gradients or curvature within different subapertures of the pupil using a WaveFront Sensor (WFS) which acquires light from a bright source, like a Natural Guide Star (NGS) or an artificial Laser Guide Star (LGS), and outputs electrical signals corresponding to the measured error. There exist different kinds of WFSs like the Shack-Hartmann, the curvature, and pyramid sensors with different methods and efficiencies in using the available photon flux to determine the wavefront error.

The data processing lets the other two sub-systems communicate by converting the error signals into wavefront correction commands (wavefront reconstruction) and by sending them to the corrector. This system, also known as Real Time Controller (RTC), is required to be powerful and fast enough to keep up with τ_0 during the AO loop.

The wavefront corrector function is to receive the reconstruction commands and correct the incoming wavefront. It usually consists of two components: a "tracking" mirror that removes the high-amplitude low-order aberrations of tip and tilt and a Deformable Mirror (DM) that corrects the high-order distortions.

In regards to the DMs, there exist different kinds depending on the technology used to deform the reflective surface: segmented, stacked array, bimorph, Micro Electro-Mechanical System (MEMS) and membrane DMs. We can also identify some notable

specifications:

- the **number of actuators** is important because, for the best correction, one should use at least one actuator per each sub-aperture of diameter r_0 by which the area of the primary mirror can be sampled; because of Eq. 2.3, the number of actuators required will be determined by the wavelength of observation;
- the **actuator pitch** is the distance between each actuator center, it is determined by the required number of actuators and the mirror's surface; this may require different kinds of technology or spatial distribution of the actuators;
- the **actuator mechanical stroke** is the displacement that each actuator can produce, it is important because a mirror needs to cope with aberrations of high amplitude; for stronger, lower order aberrations, like the tip-tilt, a dedicated separate mirror with high stroke capabilities may be required;
- a high **temporal response** is also critical, to keep up with the atmosphere variation, i.e. τ_0.

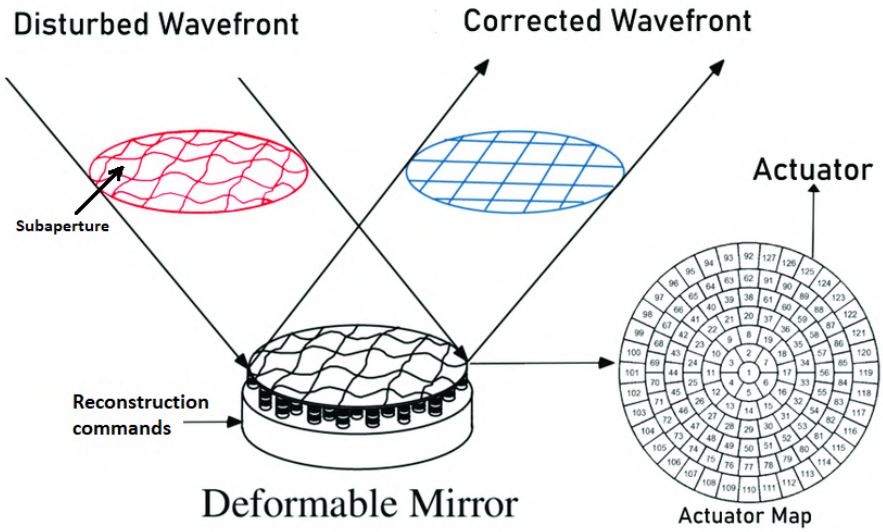

Figure 2.3: Simple scheme of a deformable mirror operating on a disturbed wavefront (credit Coronel et al. [9])

A typical AO "closed" loop starts from the wavefront correctors, which reflect the distorted wavefront into the wavefront sensor through a beam splitter. When the wavefront error is received by the RTC, simple algebra can be applied because of the linear relationship

$$A = M_{resp} \times B \tag{2.6}$$

between wavefront sensor measurement, matrix A, and correction commands, matrix B; the response or interaction matrix M_{resp} contains the coefficients that allow to go from actuators movement to desired mirror shape. In the loop, the inverse equation

$$B = M_{contr} \times A, \tag{2.7}$$

is required, where M_{contr} is called the control or reconstructor matrix which is obtained by the pseudo-inverse of M_{resp}

$$M_{contr} = M^{+}_{resp} = (M^{T}_{resp} M_{resp})^{-1} M^{T}_{resp}. \tag{2.8}$$

Once the DMs are set to the correction commands, the loop restarts to update the ever-changing distorted wavefront. A simple representation can be seen in Fig. 2.4.

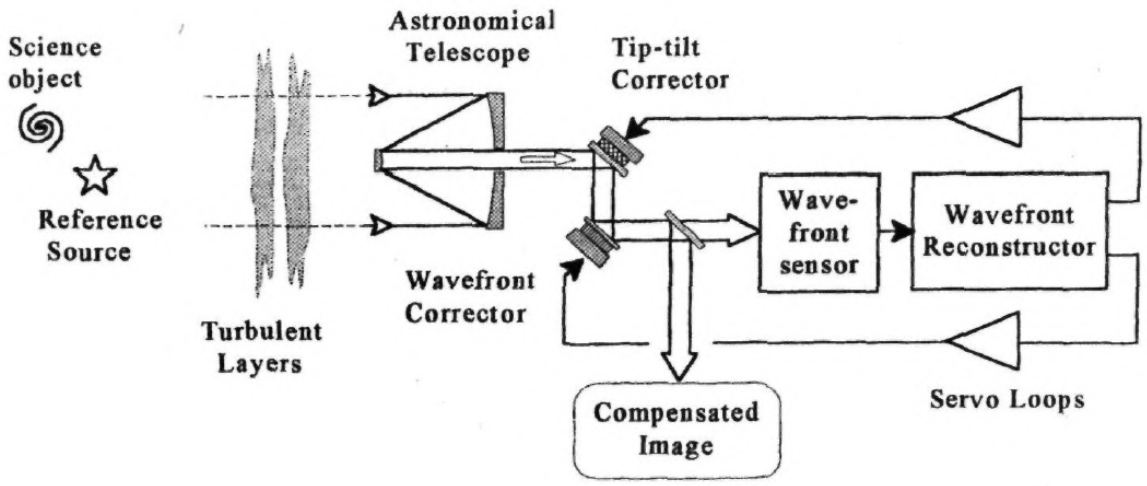

Figure 2.4: AO closed loop system from the science object to the compensated image (credits Hardy [2])

The technology of AO has various applications depending on the science targets: different wavefront sensing techniques, corrector characteristics, and computing power/timing are needed.

The simplest kind of AO is Single Conjugate Adaptive Optics (SCAO) where a single bright source is used to analyze the turbulence and will result in being able to correct only a small patch of the sky corresponding to a narrow Field Of View (FOV) (Fig. 2.5a); Multi Conjugate Adaptive Optics (MCAO), on the other hand, uses multiple sources and DMs to increase the corrected FOV by analyzing different layers of the atmosphere and working with multiple sources, most likely LGS, that cover different regions of the sky (Fig. 2.5b). When even larger FOVs are required, Multi Object Adaptive Optics (MOAO)

is used to compensate for the area around each target rather than correcting the entire sky (Fig. 2.6). In eXtreme Adaptive Optics (XAO) the goal is to resolve exoplanets around stars, reducing the scattered light through the correction of very high-order aberrations.

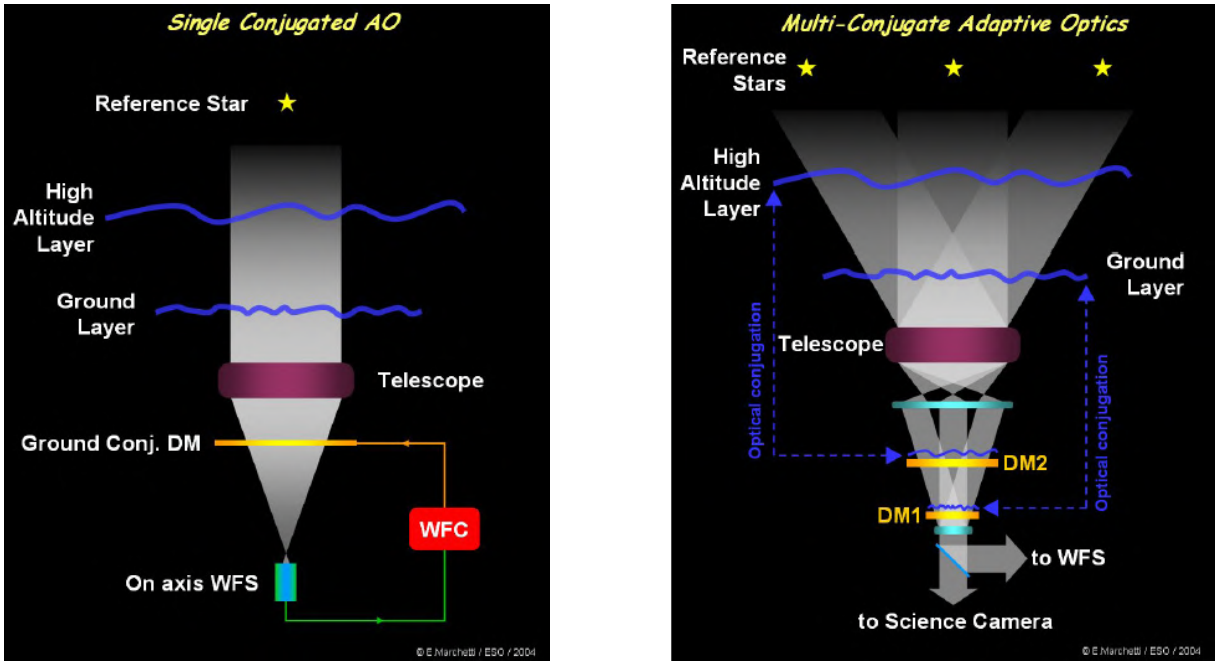

(a) (b)

Figure 2.5: Examples of SCAO on the left and MCAO on the right (credit ESO)

Of course, no AO system is "ideal" and can correct the incoming wavefront with 100% efficiency. Hence, the technical characteristics of the whole AO system must not exceed certain error budgets that depend on the type of AO technique and on the scientific goals of the instrument.

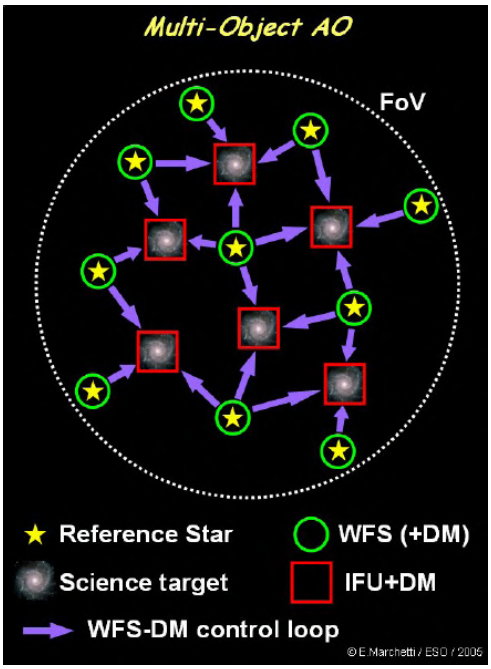

Figure 2.6: Example of a FOV used in MOAO (credit ESO)

3

Modal framework

This chapter is based on the works of Krishna and Dasari [4] and Ragazzoni [5]

Since the objective of AO is to correct a distorted wavefront, we need to be capable of mathematically describing its complex 2-dimensional functional form. This is best achieved by decomposing it through an infinite series (as in the case of Taylor and Fourier series) of (possibly orthogonal) polynomials of increasing order.

Since 1833, both geometrical and wave theories have been used by mathematicians and physicists, like Seidel, Hamilton, or Zernike, to describe the aberrations induced into a deformed wavefronts by an optical system or the atmosphere.

They started by analyzing the wavefront at the entrance pupil of a system, whose domain is $\mathbb{R}^2$, and by choosing the coordinates of the polar system (ρ, θ). In the early days, the main concern was the study of low-order aberrations (in ρ) present in small FOV telescopes and microscopes: this culminated with the results of Seidel and the classical description of low order aberrations.

Through the concept of the Eikonal equation, it was possible to research higher order modes until the introduction of aberration polynomials, which were used as polynomial bases.

3.1 Polynomial description of a wavefront

Consider a circular or annular entrance pupil represented in polar coordinates (ρ, θ) and the linear obstruction ratio ε that describe the ratio between inner and outer radii (this is zero in the case of a circular one).

This pupil can be rescaled to a unitary circle and the wavefront W reaching it can be

described as a linear combination of modes with amplitudes $c_{n,m}$:

$$W = \sum_n \sum_m c_{n,m} P_{n,m}(\rho, \theta). \tag{3.1}$$

$P_{n,m}$ are called Hamilton's polynomials[10] and are a complete set of all continuous functions on the unitary pupil; they can be written as

$$P_{n,m}(\rho, \theta) = \rho^n \cos(m\theta + \varphi), \tag{3.2}$$

where φ is the phase-lag between the entrance pupil and the focal plane of the system.

The Hamilton's polynomial base does not guarantee the orthonormality and an univocal linear combination, while the classical Zernike base does.

The Zernike polynomials[11] Z_n^m are a set that describe a circular pupil ($\varepsilon = 0$) and are presented as

$$Z_n^m = \sqrt{2(n+1)} R_n^m(\rho) \cos(m\theta + \varphi) \tag{3.3}$$

where

$$R_n^m = \sum_{s=0}^{\frac{n-m}{2}} \frac{(-1)^s (n-s)!}{s! \left[\frac{n+m}{2} - s\right]! \left[\frac{n-m}{2} - s\right]!} \rho^{n-2s} \tag{3.4}$$

In practice, since both Hamilton and Zernike bases are infinite, the decomposition is truncated to a certain point: this introduces an error which is determined by the science target and AO type.

In this thesis, I used the Zernike polynomials based on the Noll's indices[12] which use only one parameter to describe a mode: $Z_n^m \to Z_j$. The indices are calculated as

$$j = \frac{n(n+1)}{2} + |m| + \begin{cases} 0, & m > 0 \wedge n \equiv \{0, 1\} \pmod 4; \\ 0, & m < 0 \wedge n \equiv \{2, 3\} \pmod 4; \\ 1, & m \geq 0 \wedge n \equiv \{2, 3\} \pmod 4; \\ 1, & m \leq 0 \wedge n \equiv \{0, 1\} \pmod 4; \end{cases} \tag{3.5}$$

The first 17 modes, which are also used in later chapters, with their respective Noll's index and classical name can be seen in Tab. 3.1. The corresponding wavefront for each mode can be seen in Fig. 3.1 with the addition of $(n, m) \to (5, 3); (5, -3); (5, 5); (5, -5)$.

I want to end this chapter by mentioning some properties related to the usage of Zernike polynomials. It can be shown that most of the time, if the distortion of the wavefront is caused by the atmosphere or more precisely by the Kolmogorov turbulence and if the wavefront is decomposed in Zernike polynomials, the low-order aberrations

Z_n^m **(for** $\varepsilon = 0$**)**	**Noll indices**	**Classical name**
$Z_0^0 = 1$	1	Piston
$Z_1^{-1} = 2\rho \sin\theta$	3	Vertical tilt
$Z_1^1 = 2\rho \cos\theta$	2	Horizontal tilt
$Z_2^{-2} = \sqrt{6}\rho^2 \sin 2\theta$	5	Oblique astigmatism
$Z_2^0 = \sqrt{3}(2\rho^2 - 1)$	4	Defocus
$Z_2^2 = \sqrt{6}\rho^2 \cos 2\theta$	6	Vertical astigmatism
$Z_3^{-3} = \sqrt{8}\rho^3 \sin 3\theta$	9	Vertical trefoil
$Z_3^{-1} = \sqrt{8}(3\rho^2 - 2)\rho \sin\theta$	7	Vertical coma
$Z_3^1 = \sqrt{8}(3\rho^2 - 2)\rho \cos\theta$	8	Horizontal coma
$Z_3^3 = \sqrt{8}\rho^3 \cos 3\theta$	10	Oblique trefoil
$Z_4^{-4} = \sqrt{10}\rho^4 \sin 4\theta$	15	Oblique quadrafoil
$Z_4^{-2} = \sqrt{10}(4\rho^2 - 3)\rho^2 \sin 2\theta$	13	Oblique secondary astigmatism
$Z_4^0 = \sqrt{5}(6\rho^4 - 6\rho^2 + 1)$	11	Primary spherical
$Z_4^2 = \sqrt{10}(4\rho^2 - 3)\rho^2 \sin 2\theta$	12	Vertical secondary astigmatism
$Z_4^4 = \sqrt{10}\rho^4 \cos 4\theta$	14	Vertical quadrafoil
$Z_5^{-1} = \sqrt{12}(10\rho^4 - 12\rho^2 + 3)\rho \sin\theta$	17	Vertical secondary coma
$Z_5^1 = \sqrt{12}(10\rho^4 - 12\rho^2 + 3)\rho \cos\theta$	16	Horizontal secondary coma

Table 3.1: Mode indices and their classical name

present higher amplitudes, i.e. $c_{n,m}$ in Eq. 3.1.

Since the Zernike modes are not statistically represented by a descending distribution of amplitude, a different base can be introduced, the Karhunen-Loève[13]. It is constructed on the statistical properties of the Kolmogorov turbulence, which grant a descending distribution of amplitudes while also maximizing the energy in each truncated set. The Karhunen-Loève present a complex functional form and that is why Zernike is mostly used.

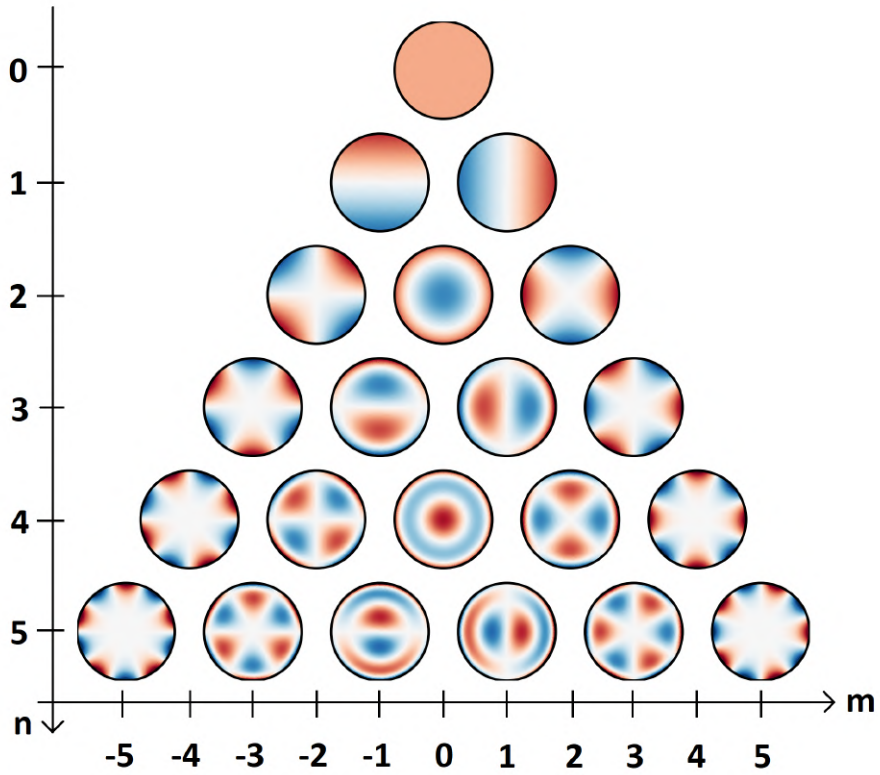

Figure 3.1: Wavefronts corresponding to each Zernike mode, where the angular index m is on the x axis and the radial index n is on the y axis

4

Assembly of an optical bench for DM characterization

A key aspect in AO is the deformable optical element capable to correct wavefronts corrupted by the atmosphere. In this chapter I am going to discuss the procedure to set up a bench to characterize a professional DM. Thanks to it, I was able to control and set any kind of shape, which in my case resulted in reaching the best possible flat surface, above the optical quality of a commercial mirror of $\lambda/10$. Now, I am going to list the main components used on the bench.

4.1 General setup

The DM that was characterized is an **ALPAO DM292** which has a pupil diameter of 26.5 mm and 292 actuators. At the end of these tests, this mirror will be used by INAF OAPd to test an AO system complete of WFS and RTC. All mirror controls can be managed by **PLICO** (Python Laboratory Instrumentation COntrol)[1], a Python suite developed by INAF - Observatory of Arcetri. The libraries that need to be used are *plico_dm_server* and *plico_dm*.

The wavefront was computed by analyzing the interference images detected by a Twyman-Green interferometer, the **PhaseCam 4030** produced by *4D technologies* whose working wavelength is 632.8 nm. This instrument is part of the equipment for studying the physics of the universe and was acquired within the Excellence projects of the Department of Physics and Astronomy "Galileo Galilei".

A Twyman-Green is a laser interferometer used to test optical systems and the wave-

[1] https://plico.readthedocs.io/en/latest/

front transmitted by them. It is a variation of the Michelson interferometer where a collimated source beam divides into two paths: a *reference beam* which is reflected on an high quality reflective surface (*reference mirror*) and a *test beam* which passes through the tested optical system and gets reflected back by a mirror at the end of the path. The interference pattern, caused by the phase variations due to the discrepancies between the tested optical system and the *reference mirror*, emerges when the two beams are recombined. At the end, the interference image is collected by a 2020×2020 pixels CCD (Fig. 4.1). The *4D PhaseCam* can be controlled manually through its own software

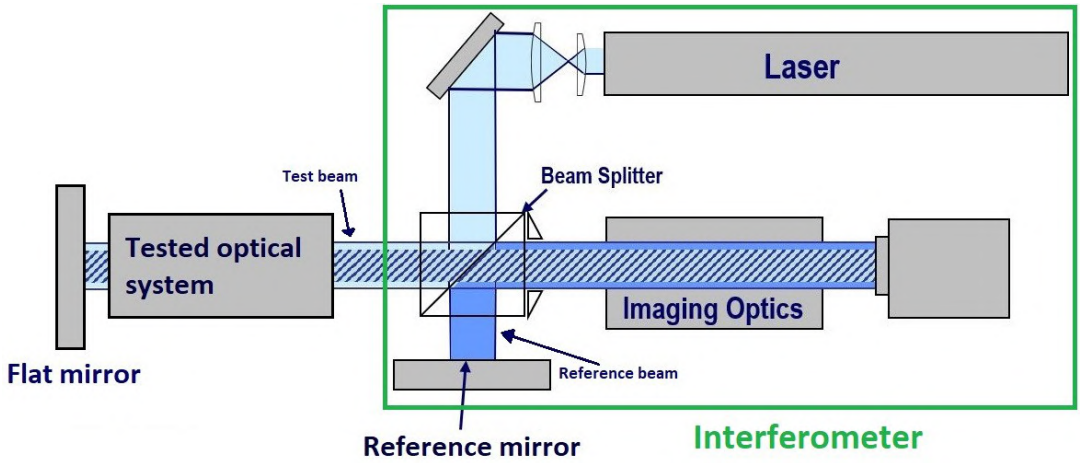

Figure 4.1: Twyman-Green Interferometer (partial credit to 4D Technology)

(*4Sight Focus*) in which, most importantly, an analysis mask can be selected to limit the surface of the captured images; in addition, interferograms can be analyzed by fitting the measured wavefront with n Zernike modes (n decided by the user - for this thesis, 11 were chosen -). This specific interferometer can also be remotely controlled using PLICO, through the library *plico_interferometer*.

Since the collimated beam exiting the interferometer is 6 mm in diameter, it would not be able to illuminate the entire DM under examination. For this reason, it had become necessary to design and construct a Beam Expander (BE) that would allow the beam to expand just beyond the diameter of the DM.

A BE can be made following the design of a refractive Galilean or Keplerian telescope. For this test, I chose a Keplerian setup that required two convex lenses, **L1** and **L2** (Fig. 4.2 and 4.7). The granted magnification M can be calculated as

$$M = \frac{f_o}{f_i} = \frac{d_o}{d_i}, \tag{4.1}$$

where f_o is the focal length of the output lens **L2**, f_i is the focal length of the input lens **L1**, d_o is the diameter of the outgoing beam and d_i the diameter of the incoming beam.

Since the DM has a diameter of 26.5 mm, the *test beam* was required to be magnified by at least a factor of 4.4.

During typical tests, the alignment of components (like the lenses of the BE) is done through a laser, which materializes the test optical path. In my case, this job was done by the interferometer beam, whose intensity was fairly low and did not allow one to visualize the back reflections and transmitted rays. For this reason I included on the setup, in autocollimation, a *flat mirror* (**Newport 20D20ER.1**) on a motorized linear stage (**Thorlabs LTS300C**) positioned at 90° with respect to the optical path, which allowed great accuracy of movements. This mirror was used as a flat $\lambda/10$ reflective surface not only during the alignment stage but also throughout the calibration tests to have a reference of the aberrations introduced by the BE optics, moving it between the BE and the DM.

4.2 First setup

For this first setup, I opted to use a f_i= 38.1 mm singlet lens (**Newport KPX079**) as **L1** and a f_o= 200 mm achromatic doublet lens (**Thorlabs AC508-200-A**) as **L2** (lenses specifications in Tab. 4.1) which gave me a **5.2x** magnification.

Before I started to setup the workbench, I had to design the BE using the OSLO ray tracing software. This helped me in figuring out the best position of the *flat mirror* and DM considering the equipment, the space available on the bench and the technical requirements of the interferometer: the *4D PhaseCam* needs to have the image plane situated 20 mm outside its frame.

After the lenses were drawn is OSLO, I fixed their separation with the addition of a perfect lens of fixed Effective Focal Length (EFL): the correction was made by finding the image focal distance that minimized the Root Mean Square (RMS) monochromatic spot size and matching it with the perfect lens focal length. To determine the place where the DM should have been located, I removed the perfect lens and placed the object plane at a distance that would give me a focal point within the length of the bench. Then I calculated the minimum RMS monochromatic spot size distance.

The resulting design can be seen in Fig. 4.2 and the focal distance of 800 mm can be easily calculated from Fig. 4.3. The fine-tuned focal distance was fixed using the focal adjustment present behind the *4D PhaseCam*.

The next step was to align the interferometer with the bench. At around 770 mm[2] from the interferometer laser output, I placed the *flat mirror* and adjusted it in the tip-tilt

[2]The conjugation of the focal point was made for the DM so extra space was required for its frame.

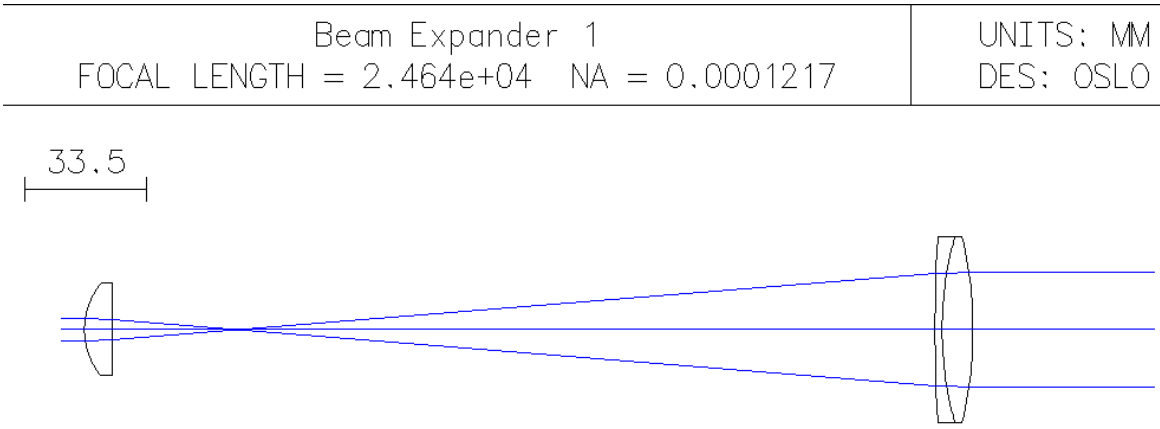

Figure 4.2: Optical design of the first BE

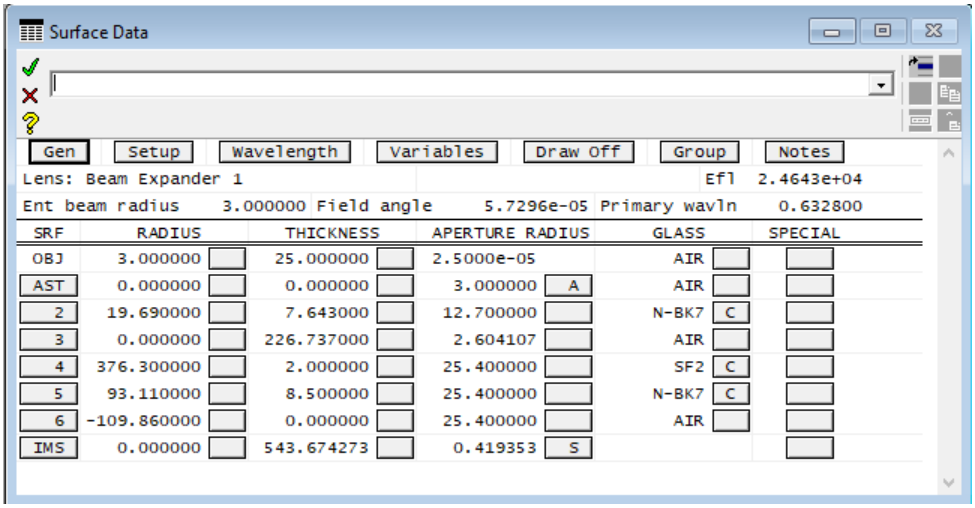

Figure 4.3: Focal point calculation for the first setup

plane, to reduce the Zernike coefficients of tilt x and tilt y, given by the analysis of the interference figure. This confirmed that the chief ray coming from the interferometer was materialized in autocollimation by the *flat mirror*.

After that, I began to construct and align the BE.

The first plano-convex singlet lens was placed at around 30 mm (as per design) from the interferometer laser output with the convex part towards it to reduce the spherical aberration introduced into the optical system. Then, I proceeded to align using the back-reflected lens spot caused by a pinhole inserted inside the collimated beam of the interferometer: adjusting the x-y plane micrometers, I made sure that the spot was going back inside the iris. Then, to fix the tip-tilt, I used the interference pattern created by the back reflections of the two surfaces of the lens and the *test beam*: the pinhole was removed, the *flat mirror* was covered with a non-reflective surface and I aligned the two vertices shown as the centers of the patterns using the tilt x and tilt y screws (Fig. 4.5).

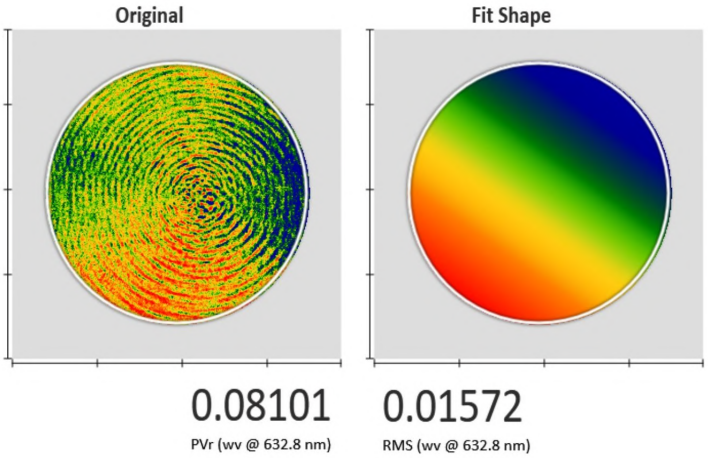

Aberration	Value [wv]
Tilt x	-0.004
Tilt y	-0.006
Defocus	-0.001
Obl. astig.	0.001
Vert. astig.	-0.009
Vert. coma	0.001
Horiz. coma	-0.001
Prim. sph.	0.001

Figure 4.4: Interferogram with Zernike coefficients and RMS of the collimated beam in wv @ 632.8 nm

During this process, I was able to determine that this lens had a wedge because, when the vertices were aligned, the interference image of both surfaces did not overlap properly.

I, then, installed the second convex doublet lens to complete the BE: it was placed at around 240 mm from the first lens because the distance of the two lenses must be the sum of their focal lengths; it was set with the larger radius surface towards the interferometer laser output to minimize the spherical aberration introduced. I proceeded with the alignment of this lens with the first one using the interference image created: I operated on the x-y plane to overlap the vertices of both lenses, which means to make the centers of both patterns coincide. After this operation, I needed to minimize the Zernike tilt x and tilt y coefficients introduced with this lens, so I adjusted the tilt x and tilt y screws of **L2** while I was offsetting the x-y micrometers (Fig. 4.5) to keep the interference pattern centered.

Once the BE was in place, I needed to fine-tune both lenses to reduce astigmatism and coma: I had to fix the decenter because these aberrations are caused by non-paraxial rays. The first step was the reduction of the x-y astigmatism: I operated the micrometers of the x-y plane of **L2**, while offsetting the tip-tilt; during this operation, I also needed to keep an eye on the focus and correct it through the z-axis micrometer. Once I was able to zero the astigmatism, I proceeded with the removal of the coma tuning the x-y plane of **L1**, offsetting its tip-tilt and correcting the focus.

At the end of this operation, I was able to reach Zernike values around 0.02 wavelengths (waves @ 632.8 nm, [wv]) for the coma, while other problems surfaced: firstly, the spherical aberration of the BE was still high (0.183 wv); secondly, although the coma was fine-tuned, the astigmatism coefficients rose up and they were difficult to correct without compromising the coma; the interference pattern created by **L1** moved out of the center

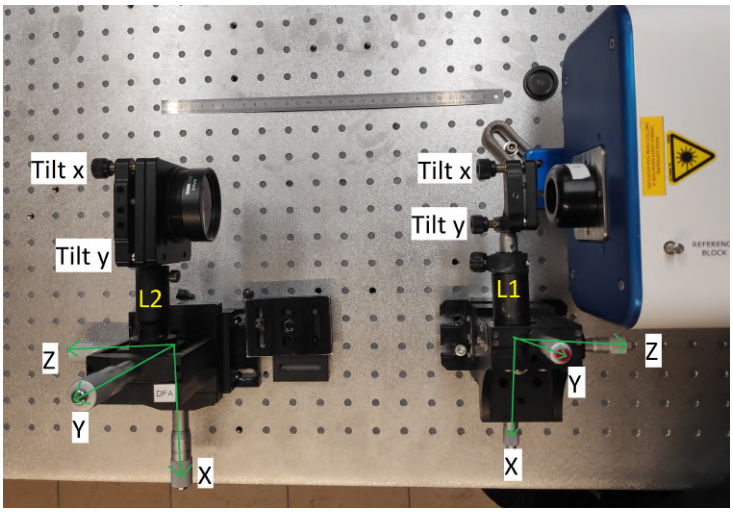

Figure 4.5: First beam expander setup

and its intensity was problematic in the analysis (the feature clearly visible on the right side of the left panel of Fig. 4.6). The high spherical aberration of the system was caused mainly by the first lens: the reason was that I chose a singlet instead of a doublet. A doublet is built with the intention of having superior control over aberrations, mainly the chromatic one, and typically has a lower spherical aberration in comparison to a singlet.

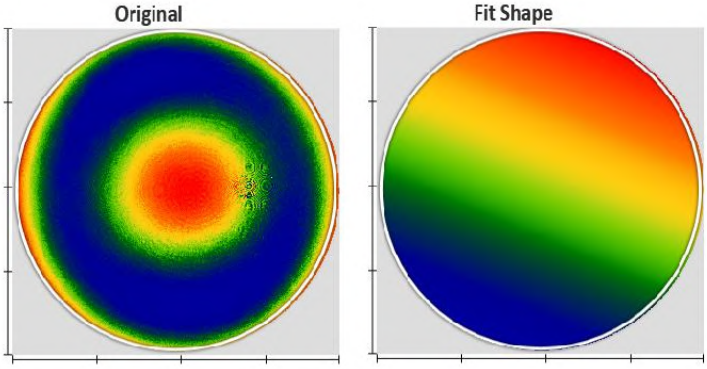

Aberration	Value [wv]
Tilt x	0.003
Tilt y	0.006
Defocus	-0.031
Obl. astig.	0.018
Vert. astig.	0.046
Vert. coma	-0.014
Horiz. coma	-0.022
Prim. sph.	0.183

Figure 4.6: Fine tuned Zernike coefficients of the first BE in wv @ 632.8 nm

The first fix I tried thinking of was the removal of the high intensity reflection introduced by **L1**: because of its vicinity with the interferometer beam, I thought of flipping it, putting the flat surface towards the interferometer; this should have worked on removing the reflections, but the spherical aberration of the BE would have increased, which was not optimal. Another option was to simply mask the spot on the pupil, like in Briguglio et al. [14], but even this solution was not possible since I wanted to keep the whole DM surface illuminated during the analysis. For this reason, I preferred to construct a better beam expander, changing both lenses.

Name	D [mm]	Material	EFL [mm]	R1 [mm]	R2 [mm]	R3 [mm]	T_c [mm]
KPX079	25.4	N-BK7	38.10	19.69	0	/	7.64
AC508-200-A	50.8	N-BK7, SF2	200.00	109.86	-93.11	-376.30	8.50 + 2.00

Table 4.1: Lenses specifications of the first setup. (D: Diameter, EFL: Effective focal length, R: Radius of curvature, T_c: Central thickness)

4.3 Second setup

Considering the problems I encountered with the first setup, especially in regard to the spherical aberrations, I opted to use two biconvex doublets: I chose **L1** with a focal length f_i= 76.2 mm (**Newport PAC046AR.14**) and **L2** with f_o= 480 mm (lenses specifications in Tab. 4.2). This resulted in a **6.3x** magnification for the BE.

The new design, with the new optics, can be seen in Fig. 4.7 and the resulting focal distance of 1000 mm, used to conjugate the DM to the required image plane position of the interferometer, can be calculated from Fig. 4.8.

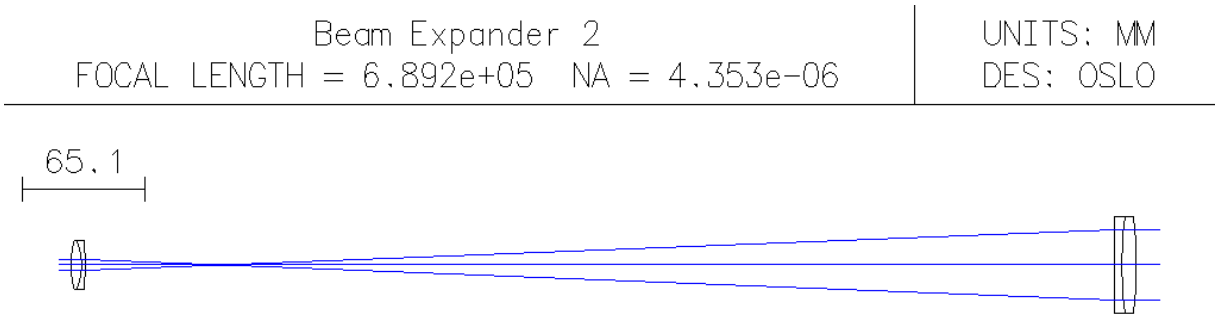

Figure 4.7: Optical design of the second BE

Since this new build required more space on the bench, I moved the *flat mirror* at around 920 mm[3] from the interferometer. Then I proceeded with the collimation of the interferometer laser, adjusting the tilt x and tilt y screws of the *flat mirror* (Fig. 4.9a).

The next step was the introduction of both lenses and their alignment.

L2 was positioned at around 650 mm from the interferometer to leave space for the first lens and the entire length of the BE; it was placed with the surface with the larger radius of curvature towards the *flat mirror* to minimize spherical aberration. To center this lens, I placed a pinhole between it and the interferometer and adjusted the x-y micrometers

[3]The conjugation of the focal point was made for the DM so extra space was required for its frame.

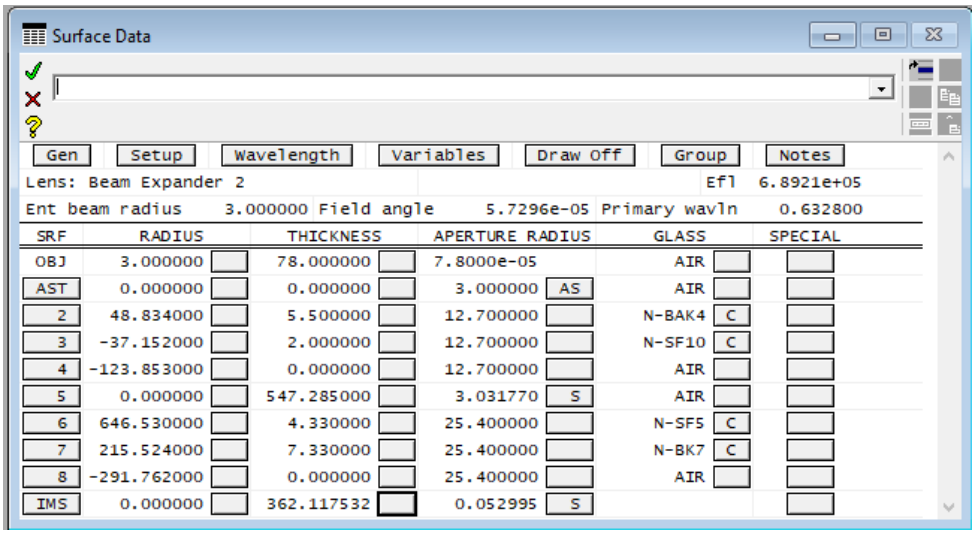

Figure 4.8: Focal point calculation for the second setup

until the reflection was pointing back inside the stop. The final position of **L2** was fixed using the interference patterns of the back reflections: I removed the pinhole, covered of the *flat mirror* and I adjusted the tilt screws, while offsetting the x-y micrometers, until the patterns of the two surfaces overlapped. To complete the beam expander, **L1** was placed 580 mm before the second lens, with the surface of larger radius of curvature towards the interferometer laser output. I set it using the back reflections: I blocked the beam behind it with a non-reflective surface and moved the lens in the x-y plane until the interference pattern was visible on the CCD; after that, I fixed the tilt overlapping the interference figures. The final position was achieved after the non-reflective surface was moved over the second lens: operating the x-y micrometers I aligned, in the best possible way, the patterns of both lenses (Fig. 4.9b).

After the construction of the BE, I dedicated myself to the fine tuning. In this new set-up, I decided to concentrate on the removal of tilt, focus and astigmatism, leaving the coma in: using the analysis of the interference image and operating the tilt and x-y-z micrometers of **L2**, I was able to reach Zernike values lower than 0.03 wv on all the targeted aberrations. The final result can be seen in Fig. 4.10: the spherical aberration of this new system resulted in 0.058 wv, which was approximately 3 times less than the first BE (0.183 wv); this set-up had a high value of coma y, which I decided not to correct during the alignment.

It was finally time to introduce the DM on the bench.

Once the *flat mirror* was moved aside, the DM was placed right behind the *flat mirror* motorized stage, at 980 mm from the interferometer; I put a pinhole around the focal point of the BE and clamped the DM frame in place once the reflected beam was going

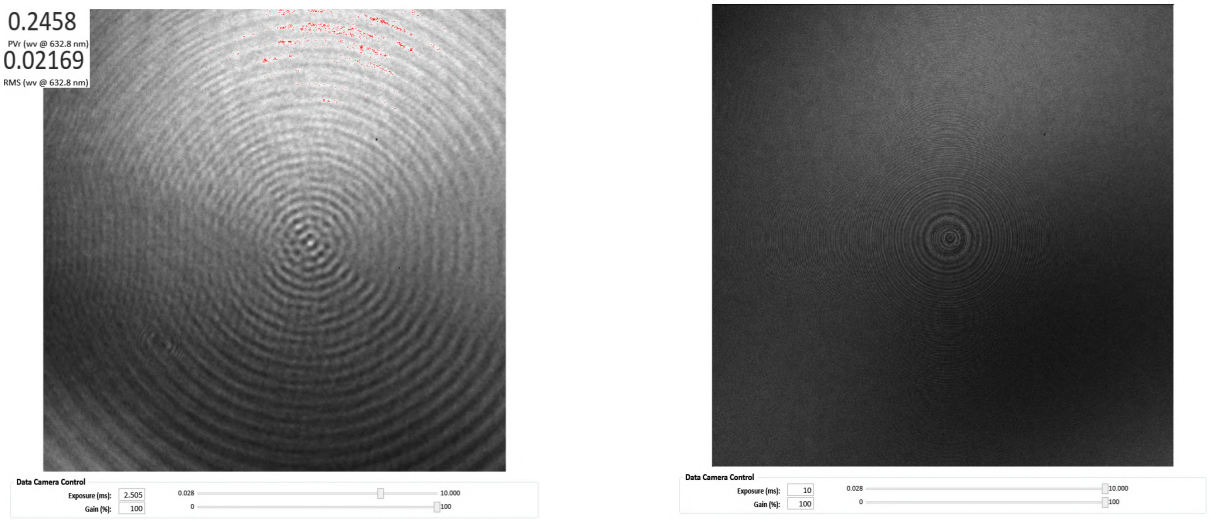

(a) (b)

Figure 4.9: Interferogram and RMS of the collimated beam in wv @ 632.8 nm (left) and aligned interference patterns of the two lenses of the second setup (right)

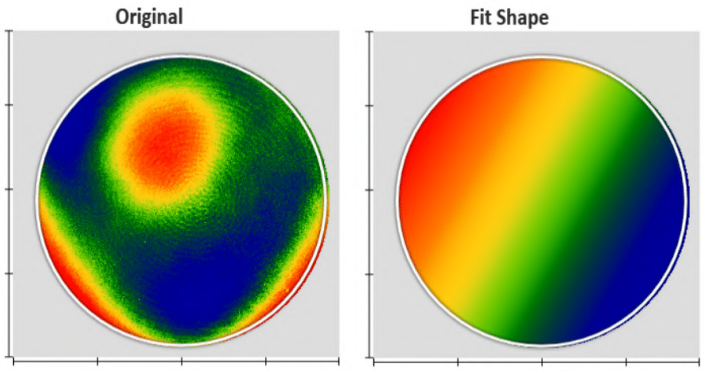

Aberration	**Value [wv]**
Tilt x	-0.013
Tilt y	0.008
Defocus	0.005
Obl. astig.	0.022
Vert. astig.	0.003
Vert. coma	-0.118
Horiz. coma	0.031
Prim. sph.	0.058

Figure 4.10: Fine tuned Zernike coefficients of the second BE setup, wv @ 632.8 nm

back inside the hole. After this operation, I fixed the tilt by adjusting its micrometers and minimizing the Zernike coefficients derived by the interference image.

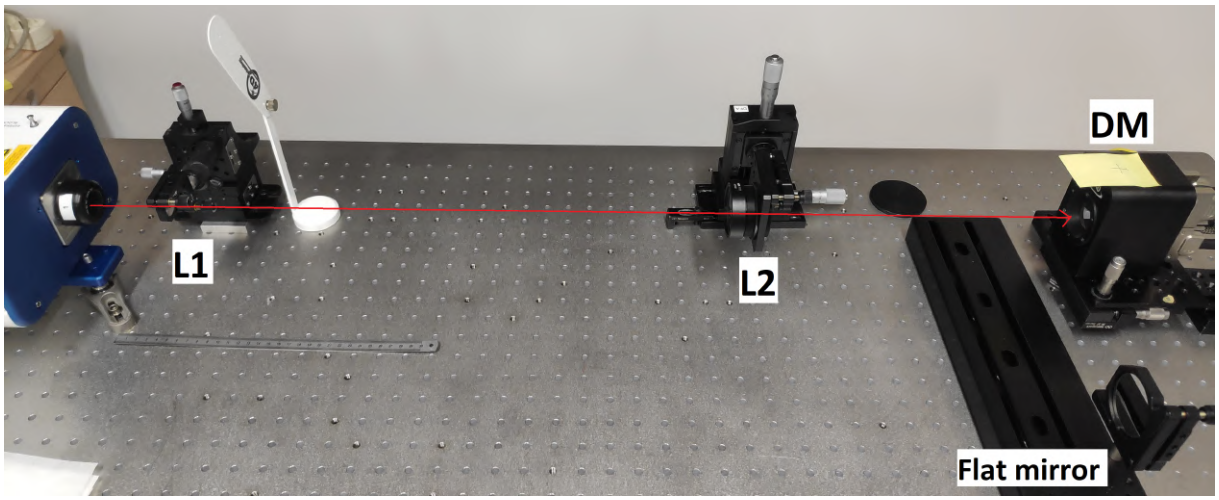

Figure 4.11: Final setup with the DM installed

Name	**D [mm]**	**Material**	**EFL [mm]**	**R1 [mm]**	**R2 [mm]**	**R3 [mm]**	**T_c [mm]**
PAC046 AR.14	25.4	N-BaK4, N-SF10	76.20	48.83	-37.15	-123.85	5.50 + 2.00
L2	50.8	N-BK7, N-SF5	480.00	291.76	-215.52	-646.53	7.33 + 4.33

Table 4.2: Lenses specifications of the second setup. (D: Diameter, EFL: Effective focal length, R: Radius of curvature, T_c: Central thickness)

4.4 Stability of the beam expander

During the construction and alignment phase, which lasted a few days, I kept seeing overnight variations of the Zernike parameters, especially the tilt x and tilt y. The main cause was the temperature fluctuations inside the laboratory (Fig. 4.12), due to the heating system that was keeping the room thermalized, which induced a tilt on the lenses. This could be explained by the type of frame used to mount the lenses: around the micrometer screws there are springs that are significantly susceptible to thermal expansion and, since the optical system was calibrated to the optimal setup in terms of aberrations, a tiny variation in decenter would induce a tilt. For this reason, I decided to check the stability of the BE, which meant a 24 hour test, where the values of the Zernike coefficients, the temperature, the pressure and the humidity of the room were collected every 5 minutes.

To gather all the information, I started writing a Python script that controlled the acquisition of interferograms and their Zernike analysis. I was able to connect to the interferometer using the PLICO library *plico_interferometer*. The temperature and pressure

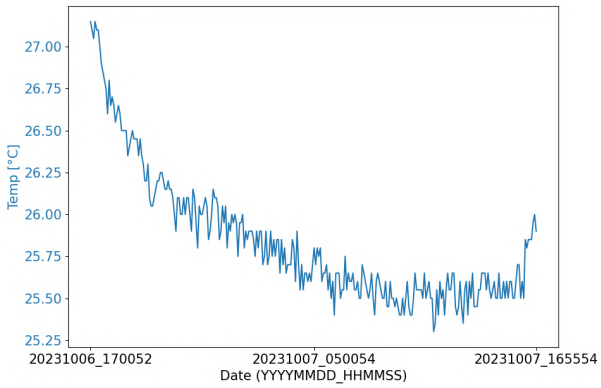

Figure 4.12: Laboratory temperatures along 24 hours

were collected using an Arduino board with two weather sensors; the values used were the average of the data collected. The humidity was supplied by a Power Distribution Unit (PDU) which had a built-in detector. The test started from the moment I left the laboratory and ran during a Saturday, which meant that no one could enter and alter the temperature of the room. Once the data was finalized, I wrote a script to print plots where on the x axis I put the time, on the right y axis the temperature, and on the left y axis I put either the Zernike coefficient values, the pressure, or the humidity.

As visible in Fig. 4.13a and 4.13b, there was a clear correlation between the variation of the temperature and the tilt. No correlation was found between temperature and the other aberrations (Fig. 4.13c→h), neither in regards to the pressure or humidity (that is why no representations are included in this thesis).

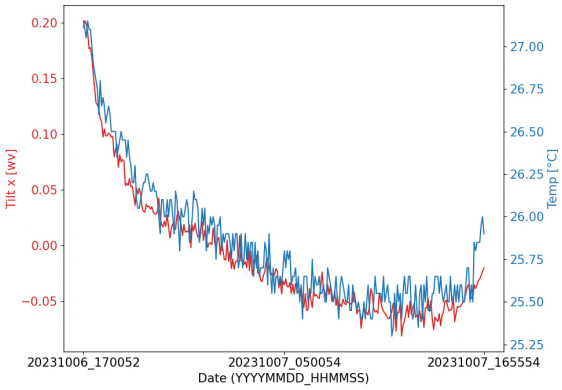

(a) Tilt x

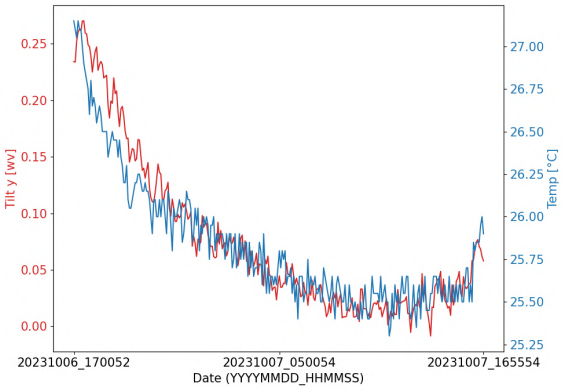

(b) Tilt y

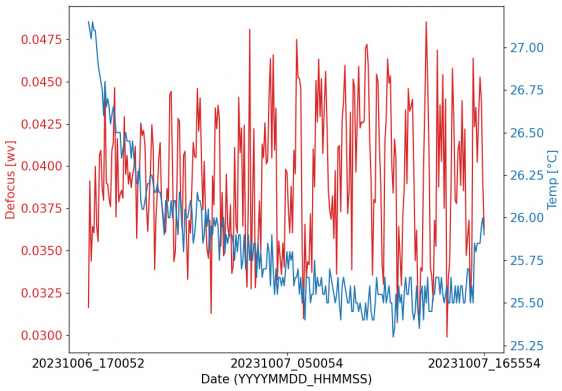

(c) Defocus

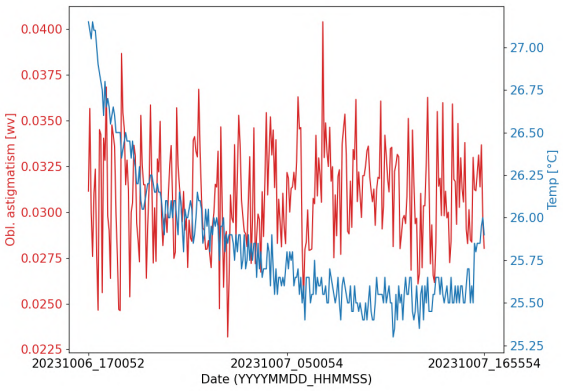

(d) Oblique astigmatism

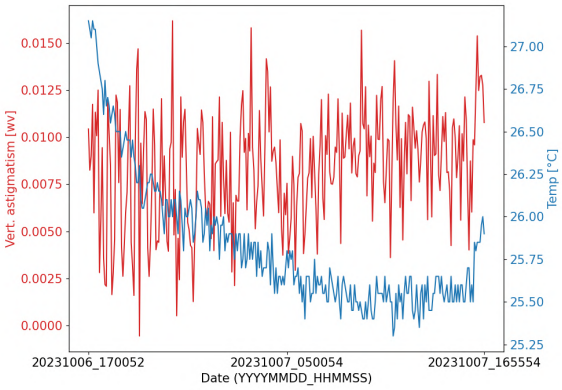

(e) Vertical astigmatism

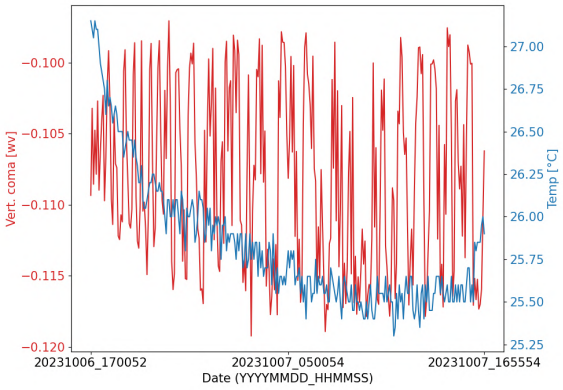

(f) Vertical coma

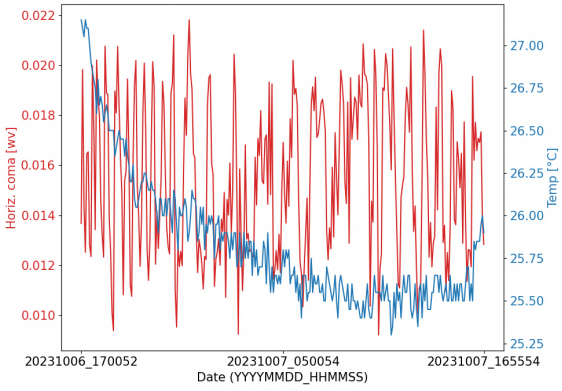

(g) Horizontal coma

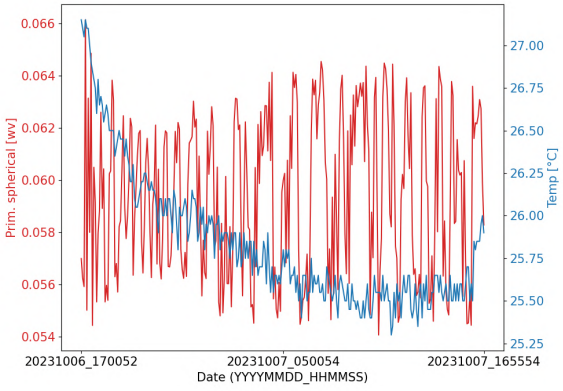

(h) Primary spherical

Figure 4.13: Stability results: Zernike coefficient values in wv (left) and temperature in °C (right) over the time of the BE stability test

5

Calibrations and analysis

In this chapter, we are going to discuss the tests that were done after the bench setup in order to achieve the characterization. I am also going to demonstrate some capabilities of the DM.

5.1 Influence function

The influence function (IF) is the response of the mirror after the activation of actuators: when a single one is used only a portion of the mirror receives a deformation and it is possible to create a *zonal IF*, if multiple actuators are triggered following some modal matrix, for example the Hadamard, the whole surface is distorted and a *modal IF* can be constructed.

To build the interaction matrix, that is the matrix that contains the coefficients to go from actuator movements to mirror shape (or wavefront), I decided to obtain a zonal IF using the *IFMaker* command of the library *plico_dm_characterization*: after all the actuators are set to their relaxed position, each one is pushed, pulled and pushed (to remove linear drift) by a preset amplitude in nanometers; 5 interferograms are then acquired and averaged for each push/pull and these data are combined to constitute the interaction matrix. The acquisition can be cycled multiple times with the resulting matrix being the average of the cycles.

I decided to calculate the first influence function with 3 cycles that lasted around 6 hours each: this introduced errors in the average due to the instability of the beam expander along the 18 hours acquisition which resulted in a non-accurate response of the DM, when later I tried to shape it in a controlled way. For this reason, I created a new and final IF using only one cycle.

After the interaction matrix was available and through the *converter* function in the library *plico_dm_characterization*, I was able to obtain the pseudo-inverse matrix to get the reconstructor matrix used to convert any wavefront shape to the relative DM commands (i.e. actuator movements).

5.2 Flattening

The next step in the characterization consisted of creating the best possible flat shape of the DM. This did not simply imply setting all the actuators to their relaxed position, instead I had to find a way to correct the "out-of-factory" mirror shape, which was not flat (Fig. 5.1).

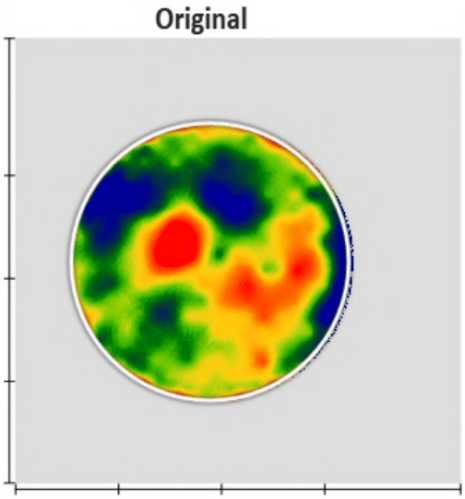

Figure 5.1: Wavefront reflected by the "out-of-factory" mirror with relaxed actuators

The idea behind it, was to measure and use the DM reflected wavefront to obtain the commands which would ensure no interference, i.e. the flat. To accomplish this task, I needed to take in consideration the presence of other optics along the optical path that introduced different aberrations to the wavefront, also known as path aberrations, which required to be isolated and subtracted during the calculation of the flat.

I proceeded following two similar paths that led to different results mostly due to the instability of the BE.

5.2.1 First flat

The first thing I did was to set up a reference interferogram of the BE[1] on the *4Sight Focus* which would be subtracted from the image acquisitions.

[1] Average of 10 interferograms using the *flat mirror*

The next steps were cycled multiple times:

- using the *flat mirror* on the stage, I acquired the average of 10 interferograms of the wavefront resulting from the beam expander (*wf_BE*);
- after the *flat mirror* was moved out of the path, the average of 10 interferograms of the wavefront reflected by the DM (*wf_DM*) was gathered;
- through the function *fromWfToDmCommand*, I calculated the actuator commands using the difference between *wf_DM* and *wf_BE*;
- the commands were subtracted from the previous position.

The first flat resulted in a wavefront RMS of 0.0760 wv, equal to 48.1 nm or $\lambda/13$; this was decent but, since the reference was taken only once and could not have been changed during the cycles, there was a propagation of errors due to the variations of the BE on the timescale of the procedure. Following a different approach, this was fixed with improved results.

Once I had the final flat (Fig. 5.2), I noticed the high peak-to-valley values at the border that compromised the RMS; I tried to use a different analysis mask which, for obvious reasons, lowered the RMS to 0.0216 wv or $\lambda/46$ for the internal surface of the DM (Fig. 5.3). The strange pattern on the border can be explained by the poor accuracy of the influence function of most external actuators. This is due to the mechanical frame holding the mirror, which partially covers the surface of the DM influenced by these actuators.

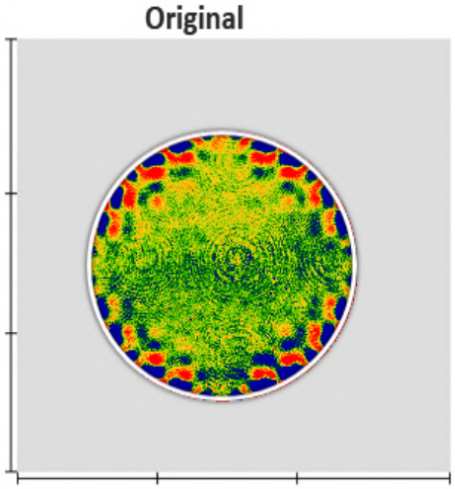

Aberration	Value [wv]
Tilt x	-0.002
Tilt y	0.008
Defocus	0.005
Obl. astig.	-0.001
Vert. astig.	-0.001
Vert. coma	0.001
Horiz. coma	0.001
Prim. sph.	0.004

Figure 5.2: First flat with RMS, PVr and table with the corresponding Zernike coefficients in wv @ 632.8 nm

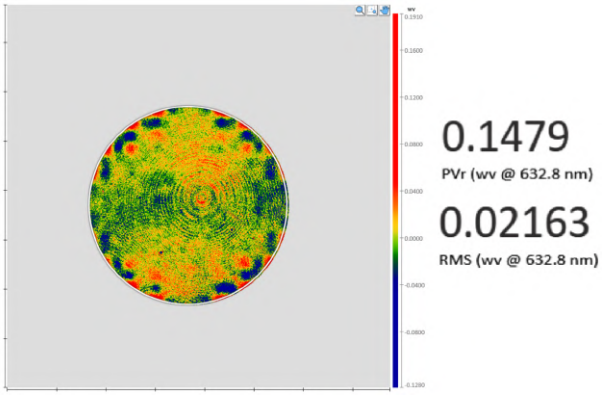

Figure 5.3: First flat with reshaped mask

5.2.2 Second flat

To address the problem resulting from the rapid change of the beam expander, I began by making the decision not to use a reference on the interferometer software. For this reason, I started by flattening the DM in a way that would compensate both the aberrations introduced by the BE and the relaxed mirror shape:

a) the average of 10 interferograms was acquired (*wf*);

b) *wf* was converted into DM commands;

c) the commands were subtracted from the previous position.

These tasks were repeated multiple times until I reached the pattern seen in Fig. 5.4a.

To gather the proper flat, this is how I proceeded:

d) the *flat mirror* was brought in front of the DM;

e) the average of 10 interferograms was collected (*wf_BE*);

f) the DM commands calculated using *wf_BE* were added to the previous flattening.

The addition was made because the starting flat was the result of the sum of the "proper flat" and the inverse aberrations introduced by the BE.

The RMS of the flat was finally calculated using the numpy standard deviation of the difference between the wavefront of the final flat shape of DM and the BE (*wf_BE*) (see Fig. 5.4b).

The result was a RMS of 0.0500 wv, equal to 31.6 nm or a surface imperfection of $\lambda/20$.

Similar edge problems were noticed during this process.

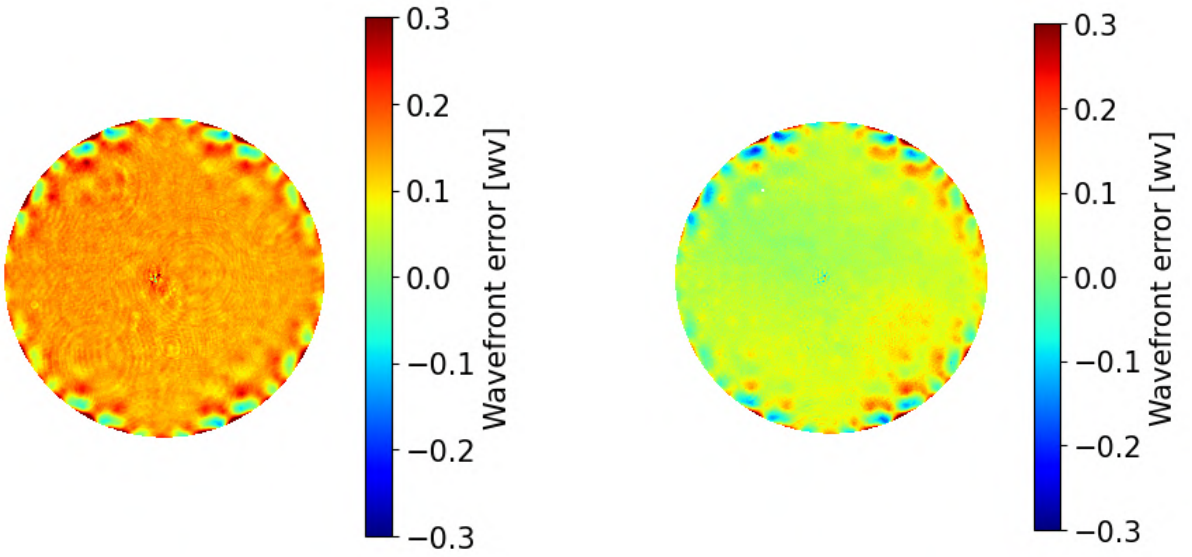

(a) (b)

Figure 5.4: Flat wavefront resulting from flattening cycles (a→c) (left) and the wavefront resulting from the best flat shape of the mirror (d→f) (right), wv @ 632.8 nm

5.2.3 Improved second flat

As a last test, to go beyond the limit of $\lambda/20$ that I was trying to reach, I moved the DM292 in front of a laser interferometer produced by *Zygo* which has a testing beam diameter that is larger than the mirror itself. This meant that no beam expander was needed for the analysis and no constant variations of aberration coefficients would be needed to be taken in consideration.

After the mirror was accurately aligned in front of the interferometer, the previously taken flat was set and, through a Python script, I tried to manually correct all the residual higher amplitude aberrations (from low to high order) that were not properly corrected, mainly because of the presence of the beam expander, by adding or subtracting them from the flat shape commands.

By the end, the entire mirror surface reached an astonishing RMS of 0.0230 wv corresponding to 14.6 nm or $\lambda/43$. This result can be seen in 5.5.

5.3 Stroke linearity

To have full control and understanding of the deformable mirror I was working with, one last test was needed, during which I checked the linearity of the actuator stroke. The goal was to verify the linear response of the displacement after a certain linear input is given and to verify that there were no correlations between aberrations.

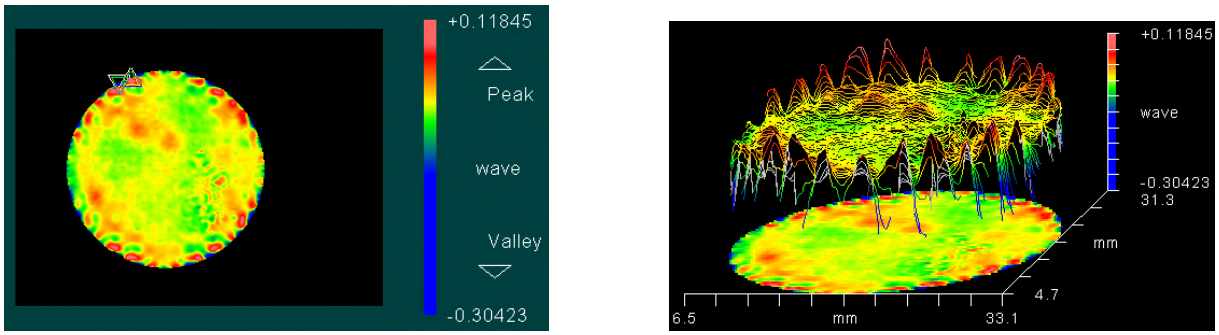

Figure 5.5: Flat resulting from the manual correction of the previously take flat of $\lambda/20$ in 2D (left) and 3D (right)

To verify linearity, first I created a command matrix for the first 17 Zernike modes, excluding the piston, using the *plico_dm_characterization* library: this matrix contained the actuator commands to apply different aberrations. The next step was to find 20 evenly distributed amplitudes for each mode in a way that would have not broken the mirror; in other words, choosing a range in which the commands needed to push such amplitude would not surpass a critical value. Then, each aberration was applied to the DM set to its relaxed position, instead of the flat previously taken, because I found some hysteresis problems at the end of each application due to the strong amplitudes, which caused the flat shape to not be flat anymore.

At the end of the test, I was able to collect all the Zernike coefficients for each implemented mode and construct a plot proving the linear response given an input of linear increment of amplitudes. This can be seen in the following pages (Fig. 5.6) where I also added a table showing the response, with the average and RMS, of the other aberration during the test of each mode proving no correlation between modes.

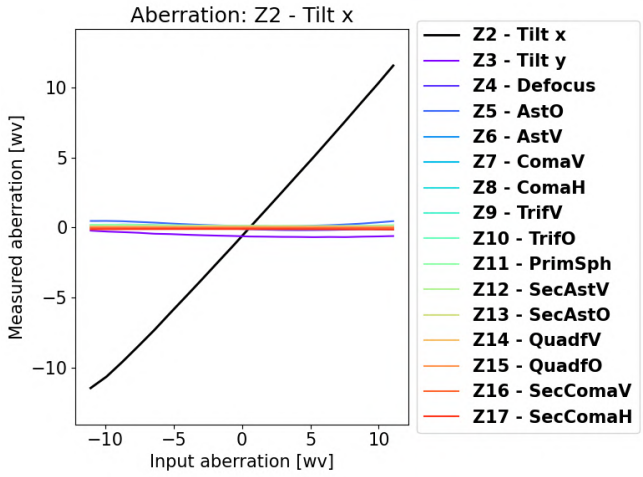

Aber	Avr ± rms [wv]		
Z3	-0.543 ± 0.142	Z11	0.147 ± 0.040
Z4	-0.013 ± 0.140	Z12	0.110 ± 0.018
Z5	0.263 ± 0.136	Z13	-0.094 ± 0.001
Z6	-0.060 ± 0.032	Z14	0.072 ± 0.003
Z7	-0.020 ± 0.011	Z15	0.008 ± 0.015
Z8	0.020 ± 0.029	Z16	-0.024 ± 0.005
Z9	-0.018 ± 0.008	Z17	-0.113 ± 0.010
Z10	0.068 ± 0.046		

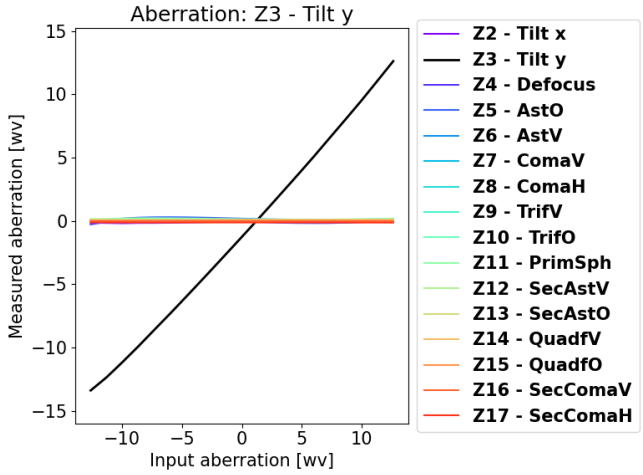

Aber	Avr ± rms [wv]		
Z2	-0.055 ± 0.089	Z11	0.150 ± 0.038
Z4	-0.018 ± 0.143	Z12	0.108 ± 0.014
Z5	0.154 ± 0.096	Z13	-0.097 ± 0.006
Z6	-0.060 ± 0.007	Z14	0.067 ± 0.012
Z7	0.006 ± 0.025	Z15	0.008 ± 0.004
Z8	-0.003 ± 0.005	Z16	-0.011 ± 0.008
Z9	-0.018 ± 0.003	Z17	-0.125 ± 0.005
Z10	0.063 ± 0.017		

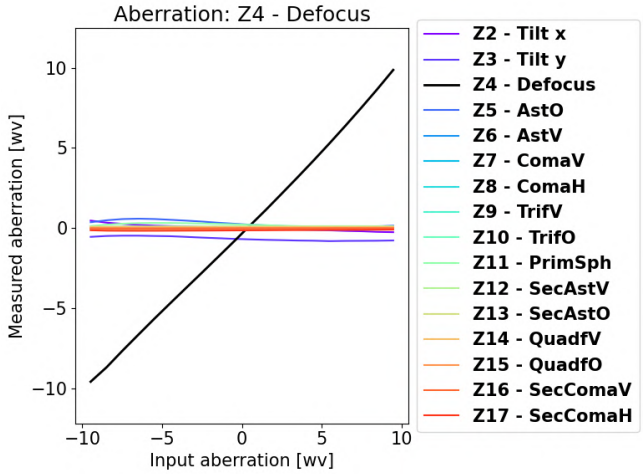

Aber	Avr ± rms [wv]		
Z2	0.018 ± 0.190	Z11	0.178 ± 0.104
Z3	-0.659 ± 0.126	Z12	0.091 ± 0.024
Z5	0.286 ± 0.187	Z13	-0.096 ± 0.003
Z6	-0.071 ± 0.017	Z14	0.074 ± 0.006
Z7	-0.010 ± 0.005	Z15	0.003 ± 0.006
Z8	-0.006 ± 0.011	Z16	-0.023 ± 0.006
Z9	-0.019 ± 0.004	Z17	-0.138 ± 0.023
Z10	0.071 ± 0.020		

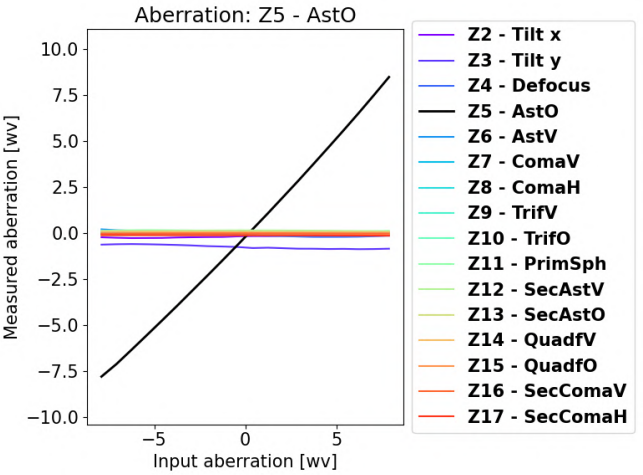

Aber	Avr ± rms [wv]		
Z2	-0.190 ± 0.048	Z11	0.120 ± 0.026
Z3	-0.749 ± 0.103	Z12	0.131 ± 0.017
Z4	-0.073 ± 0.109	Z13	-0.106 ± 0.007
Z6	0.045 ± 0.060	Z14	0.068 ± 0.008
Z7	-0.005 ± 0.008	Z15	-0.020 ± 0.026
Z8	0.011 ± 0.011	Z16	-0.017 ± 0.001
Z9	-0.008 ± 0.010	Z17	-0.117 ± 0.010
Z10	0.052 ± 0.023		

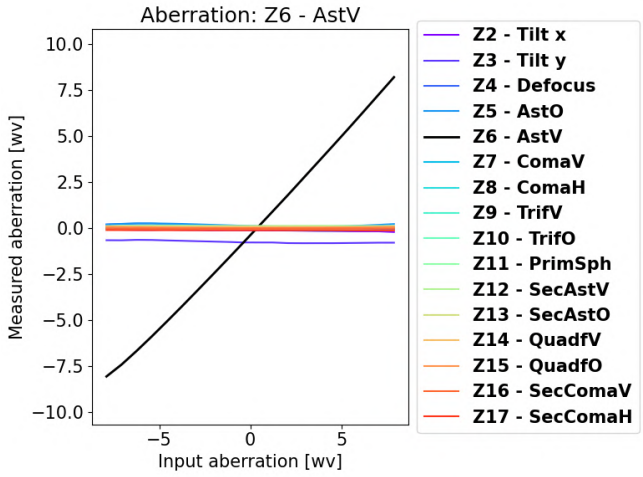

Aber	Avr ± rms [wv]		
Z2	-0.126 ± 0.036	Z11	0.109 ± 0.023
Z3	-0.746 ± 0.064	Z12	0.114 ± 0.010
Z4	0.026 ± 0.147	Z13	-0.077 ± 0.021
Z5	0.167 ± 0.060	Z14	0.071 ± 0.013
Z7	-0.009 ± 0.006	Z15	0.033 ± 0.024
Z8	0.003 ± 0.009	Z16	-0.016 ± 0.001
Z9	-0.019 ± 0.026	Z17	-0.115 ± 0.005
Z10	0.054 ± 0.023		

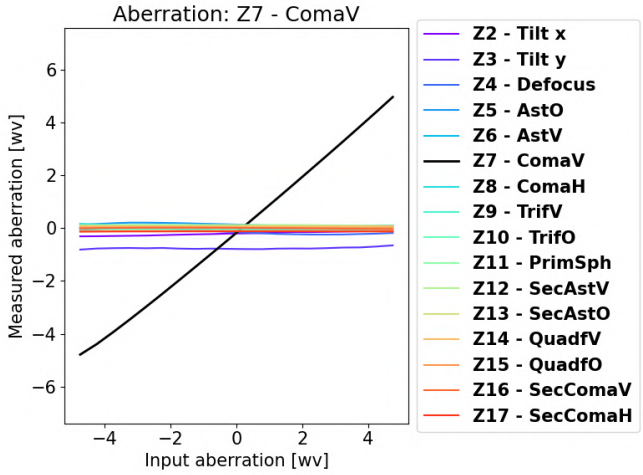

Aber	Avr ± rms [wv]		
Z2	-0.206 ± 0.070	Z11	0.100 ± 0.018
Z3	-0.760 ± 0.035	Z12	0.107 ± 0.011
Z4	-0.134 ± 0.090	Z13	-0.097 ± 0.002
Z5	0.132 ± 0.047	Z14	0.069 ± 0.001
Z6	-0.049 ± 0.029	Z15	0.006 ± 0.003
Z8	0.068 ± 0.036	Z16	-0.001 ± 0.019
Z9	-0.014 ± 0.015	Z17	-0.126 ± 0.003
Z10	0.046 ± 0.008		

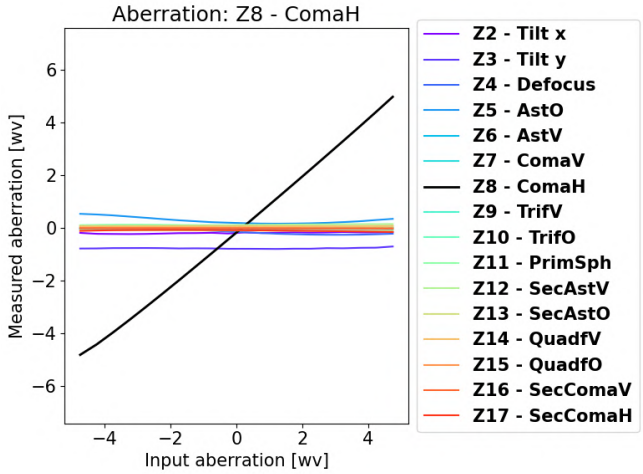

Aber	Avr ± rms [wv]		
Z2	-0.188 ± 0.024	Z11	0.096 ± 0.020
Z3	-0.769 ± 0.020	Z12	0.116 ± 0.022
Z4	-0.126 ± 0.112	Z13	-0.096 ± 0.008
Z5	0.292 ± 0.118	Z14	0.066 ± 0.004
Z6	-0.035 ± 0.007	Z15	0.002 ± 0.004
Z7	-0.003 ± 0.011	Z16	-0.015 ± 0.004
Z9	-0.018 ± 0.004	Z17	-0.099 ± 0.024
Z10	0.042 ± 0.013		

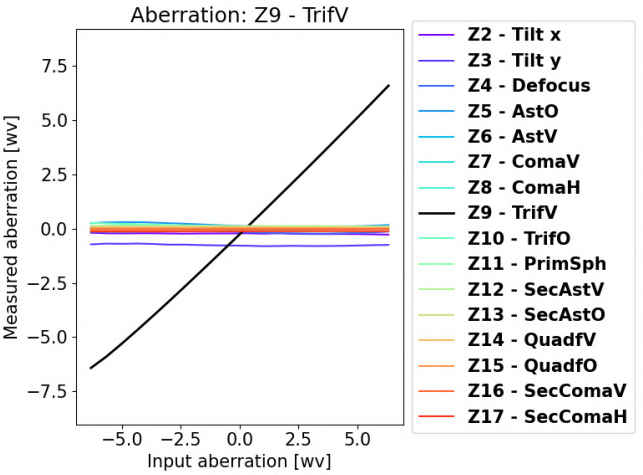

Aber	Avr ± rms [wv]		
Z2	-0.227 ± 0.020	Z11	0.112 ± 0.024
Z3	-0.756 ± 0.039	Z12	0.116 ± 0.006
Z4	-0.121 ± 0.082	Z13	-0.094 ± 0.007
Z5	0.174 ± 0.081	Z14	0.068 ± 0.008
Z6	-0.065 ± 0.050	Z15	0.006 ± 0.004
Z7	0.006 ± 0.004	Z16	-0.020 ± 0.005
Z8	0.018 ± 0.003	Z17	-0.117 ± 0.005
Z10	0.135 ± 0.061		

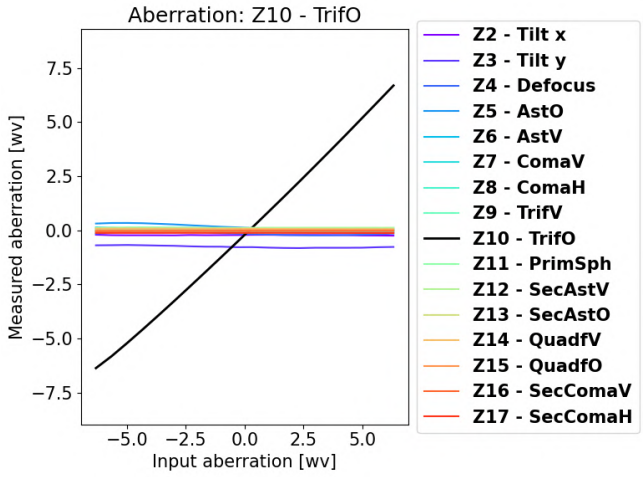

Aber	Avr ± rms [wv]		
Z2	-0.221 ± 0.011	Z11	0.109 ± 0.019
Z3	-0.757 ± 0.047	Z12	0.113 ± 0.010
Z4	-0.141 ± 0.071	Z13	-0.096 ± 0.005
Z5	0.167 ± 0.111	Z14	0.070 ± 0.009
Z6	-0.053 ± 0.011	Z15	0.006 ± 0.005
Z7	0.054 ± 0.033	Z16	-0.026 ± 0.006
Z8	0.022 ± 0.004	Z17	-0.119 ± 0.003
Z9	-0.014 ± 0.008		

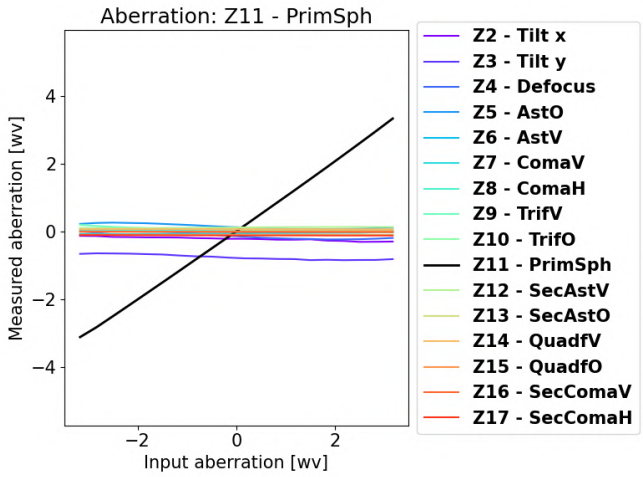

Aber	Avr ± rms [wv]		
Z2	-0.219 ± 0.053	Z10	0.065 ± 0.017
Z3	-0.758 ± 0.074	Z12	0.115 ± 0.013
Z4	-0.125 ± 0.092	Z13	-0.097 ± 0.001
Z5	0.149 ± 0.070	Z14	0.066 ± 0.002
Z6	-0.056 ± 0.017	Z15	-0.002 ± 0.006
Z7	0.007 ± 0.004	Z16	-0.014 ± 0.006
Z8	0.016 ± 0.026	Z17	-0.115 ± 0.004
Z9	0.067 ± 0.049		

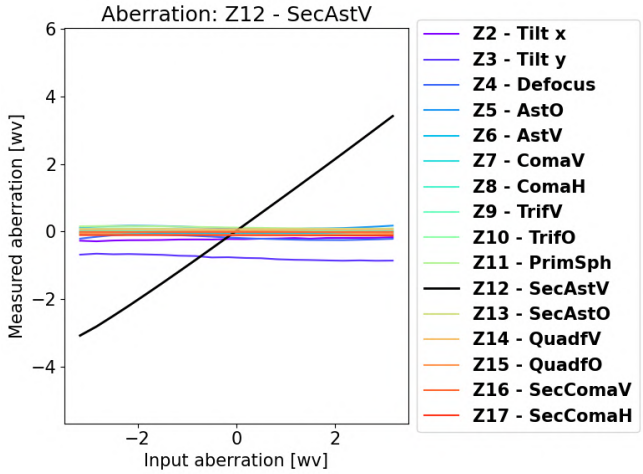

Aber	Avr ± rms [wv]		
Z2	-0.227 ± 0.033	Z10	0.046 ± 0.036
Z3	-0.772 ± 0.075	Z11	0.120 ± 0.030
Z4	-0.184 ± 0.060	Z13	-0.096 ± 0.002
Z5	0.122 ± 0.033	Z14	0.065 ± 0.001
Z6	-0.055 ± 0.003	Z15	-0.021 ± 0.024
Z7	0.005 ± 0.005	Z16	-0.015 ± 0.001
Z8	0.019 ± 0.039	Z17	-0.111 ± 0.005
Z9	0.008 ± 0.015		

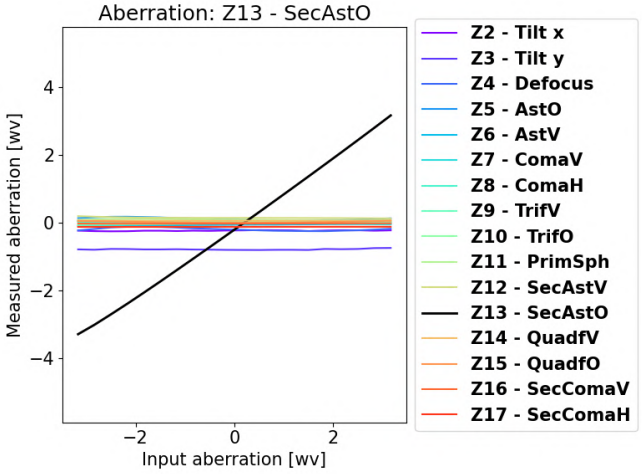

Aber	Avr ± rms [wv]		
Z2	-0.227 ± 0.010	Z10	0.043 ± 0.010
Z3	-0.779 ± 0.017	Z11	0.095 ± 0.016
Z4	-0.185 ± 0.043	Z12	0.154 ± 0.016
Z5	0.120 ± 0.038	Z14	0.066 ± 0.001
Z6	-0.055 ± 0.019	Z15	0.028 ± 0.020
Z7	0.006 ± 0.031	Z16	-0.017 ± 0.004
Z8	0.018 ± 0.006	Z17	-0.114 ± 0.002
Z9	-0.011 ± 0.031		

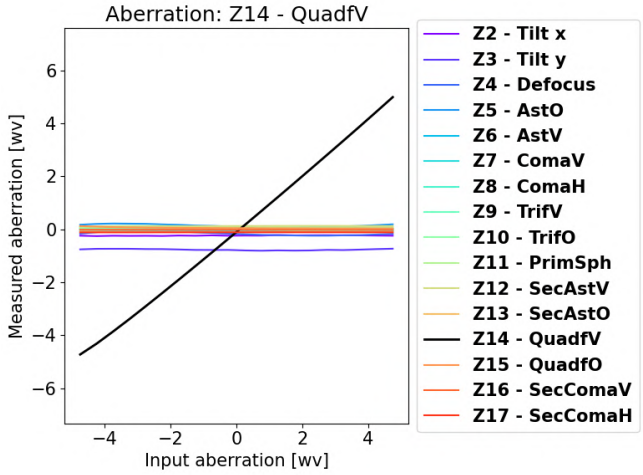

Aber	Avr ± rms [wv]		
Z2	-0.227 ± 0.010	Z10	0.043 ± 0.010
Z3	-0.779 ± 0.017	Z11	0.095 ± 0.016
Z4	-0.185 ± 0.043	Z12	0.154 ± 0.016
Z5	0.120 ± 0.038	Z14	0.066 ± 0.001
Z6	-0.055 ± 0.019	Z15	0.028 ± 0.020
Z7	0.006 ± 0.031	Z16	-0.017 ± 0.004
Z8	0.018 ± 0.006	Z17	-0.114 ± 0.002
Z9	-0.011 ± 0.031		

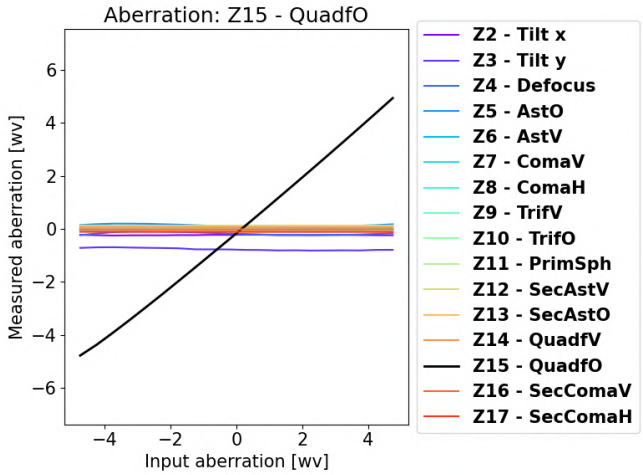

Aber	Avr ± rms [wv]		
Z2	-0.234 ± 0.008	Z10	0.045 ± 0.032
Z3	-0.768 ± 0.044	Z11	0.094 ± 0.012
Z4	-0.176 ± 0.049	Z12	0.124 ± 0.004
Z5	0.133 ± 0.043	Z13	-0.066 ± 0.020
Z6	-0.057 ± 0.006	Z14	0.066 ± 0.004
Z7	0.001 ± 0.008	Z16	-0.016 ± 0.001
Z8	0.012 ± 0.003	Z17	-0.114 ± 0.001
Z9	-0.009 ± 0.008		

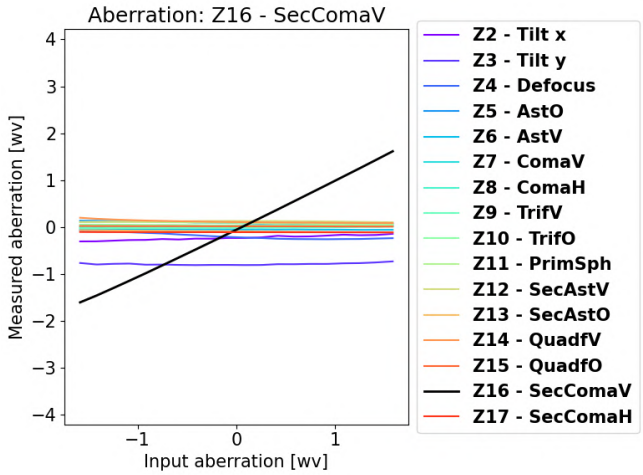

Aber	Avr ± rms [wv]		
Z2	-0.231 ± 0.048	Z10	0.037 ± 0.007
Z3	-0.790 ± 0.020	Z11	0.085 ± 0.018
Z4	-0.194 ± 0.063	Z12	0.117 ± 0.009
Z5	0.091 ± 0.026	Z13	-0.093 ± 0.014
Z6	-0.054 ± 0.004	Z14	0.116 ± 0.031
Z7	0.006 ± 0.01	Z15	0.015 ± 0.003
Z8	0.016 ± 0.002	Z17	-0.112 ± 0.002
Z9	-0.014 ± 0.010		

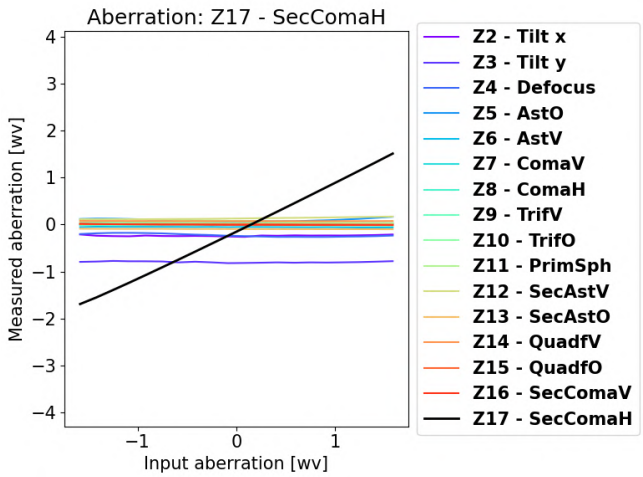

Aber	Avr ± rms [wv]		
Z2	-0.236 ± 0.012	Z10	0.033 ± 0.009
Z3	-0.797 ± 0.013	Z11	0.074 ± 0.029
Z4	-0.226 ± 0.032	Z12	0.134 ± 0.019
Z5	0.100 ± 0.028	Z13	-0.094 ± 0.003
Z6	-0.053 ± 0.005	Z14	0.074 ± 0.001
Z7	0.004 ± 0.006	Z15	0.006 ± 0.004
Z8	0.020 ± 0.008	Z16	-0.003 ± 0.008
Z9	-0.013 ± 0.005		

Figure 5.6: Stroke linearity and tables with the averages and RMS, in wv @ 632.8 nm, of the other aberrations during the test

5.4 Aberrations on the PSF

Since the calibration and characterization were finished, I wanted to demonstrate some capabilities of the DM292. I started by showing the first 17 Zernike modes set on the mirror and their corresponding aberrated PSF.

To achieve this, I had to create a second optical path, reflected by the DM, that simulated a scientific branch affected by non-common path aberrations: a 5 μm Pellicular Beam Splitter (PBS)(**Newport PBS-2**)[2] was placed between **L2** and the mirror, it was followed by a 500 mm focal length doublet lens (**Thorlabs AC508-500-A**)[3] and trailed by a CMOS camera (**ZWO ASI183MM**) placed at the lens focal point (Fig. 5.7b). The decision of using a pellicular beam splitter, instead of a cubic one, was made because it was the only larger enough to cover the DM surface diameter. This came with some setbacks as this PBS introduced a wavefront error of 1 wave per 50.8 mm of diameter, adding both common and non-common path aberrations. Still, these components were chosen in a way that the aberrations introduced would be minimal.

The PBS and the lens were aligned using a diode laser located on the camera position (Fig. 5.7a). The beam splitter was placed at 45° with respect to the *test beam* and it was aligned making sure that the diode laser reflection, made by the DM, were going back inside the interferometer; the lens location was fixed using the back reflections and the transmitted rays. Once the diode laser was remove, I mounted the camera around the lens focal distance and fine tuned its position by minimizing the diameter of the PSF.

To set a particular aberration, I used the previously calculated command matrix for the first 17 Zernike modes, excluding the piston. Each mode was added to the shape of the mirror in which the BE and PBS wavefronts were not reflected: this meant that I had to set a flat shape that would correct the "out-of-factory", BE and PBS introduced aberrations (Fig. 5.8).

In the next pages, the wavefront reflected by the DM is accompanied by the Zernike values, in wv @ 632.8 nm, in the Noll notation and the corresponding PSF is shown using a logarithmic filter for a better visibility.

Some considerations need to be taken into account:

- because the PBS was dirty and there was no possibility of cleaning it, the interferograms are presented with a white feature at their center;
- due to the fact that the new optical branch was illuminated by coherent monochromatic light, the PSFs were affected by interference patterns;

[2] Working wavelength range 375-2400 nm
[3] Technical specifications in Tab. 5.1

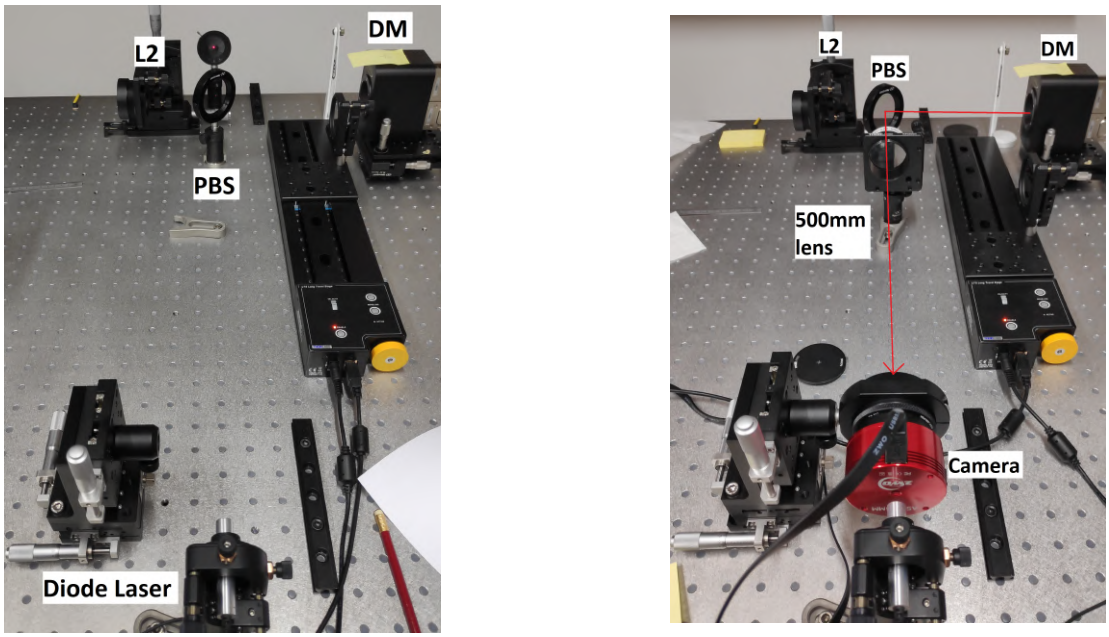

(a) (b)

Figure 5.7: Laser alignment of the PBS (left) and final setup (right)

- since the PBS reflected wavefront introduced aberrations in the new optical path, which were not possible to be eliminated, the PSFs are affected by residual aberrations as clearly seen in Fig. 5.10b, as the defocus is non-circular and affected by astigmatism.

Name	**D [mm]**	**Material**	**EFL [mm]**	**R1 [mm]**	**R2 [mm]**	**R3 [mm]**	**T_c [mm]**
AC508-500-A	50.8	N-BAK4, N-SF10	500	272.9	-234.3	-970.0	5.0 + 2.0
PBS-2	51.6	Polymer film	/	/	/	/	/

Table 5.1: Technical specifications (D: Diameter, EFL: Effective focal length, R: Radius of curvature, T_c: Central thickness)

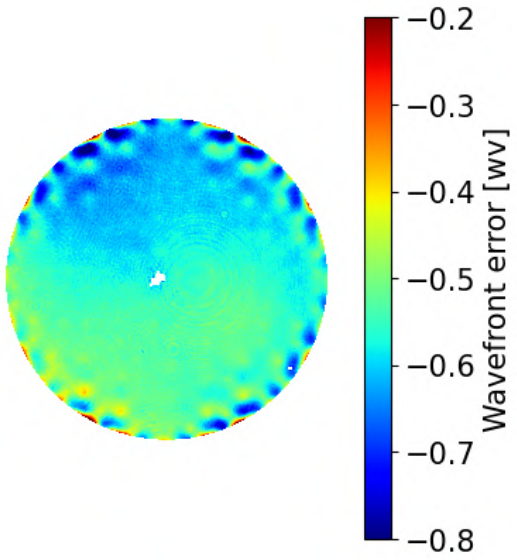

Aberration	Value [wv]
Tilt x	-0.005
Tilt y	0.035
Defocus	0.004
Obl. astig.	-0.013
Vert. astig.	0.005
Vert. coma	-0.008
Horiz. coma	-0.008
Prim. sph.	0.008

Figure 5.8: Flat with RMS = 0.055 wv and table with its aberrations

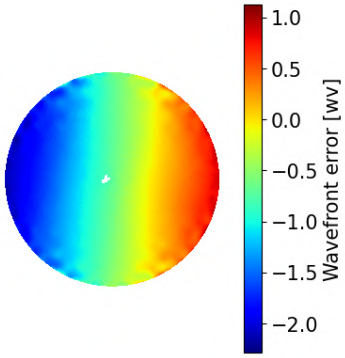

(a) Tilt x = 0.784 wv

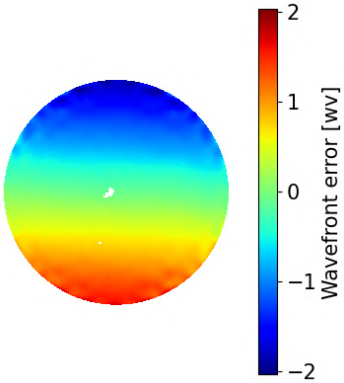

(b) Tilt y = 0.893 wv

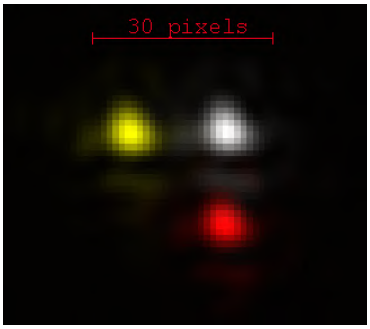

(c) PSFs

Figure 5.9: Interferograms of tilt x-y and combination of the PSFs (flat = white, titlt x = yellow, tilt y = red)

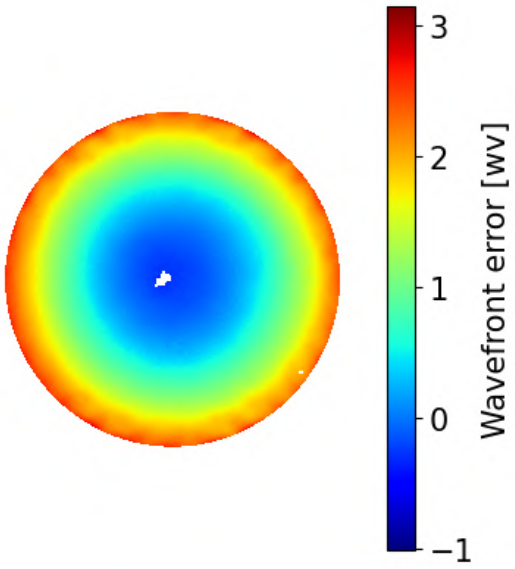

(a) Defocus = 0.792 wv

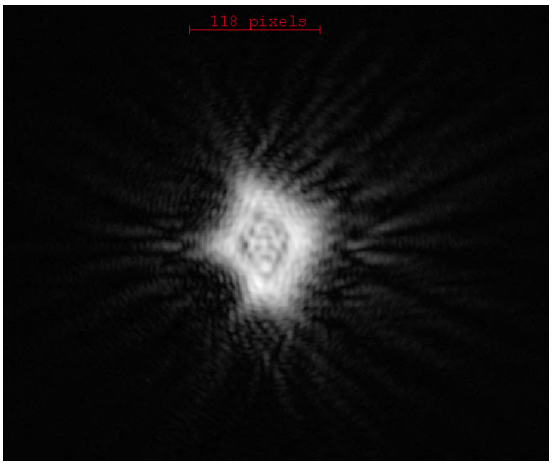

(b) PSF

Figure 5.10: Interferogram of the defocus and its PSF

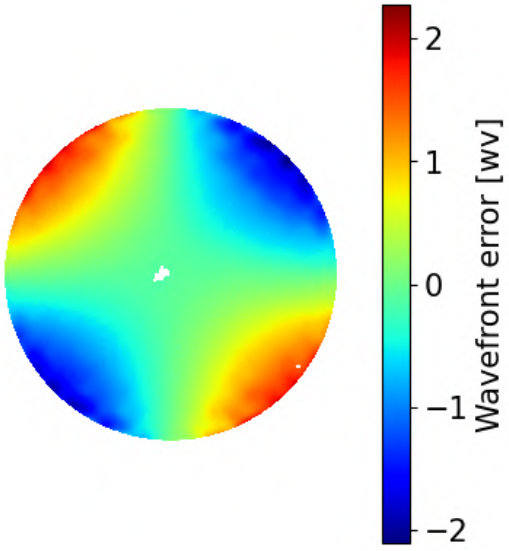

(a) Obl. astig. = 0.791 wv

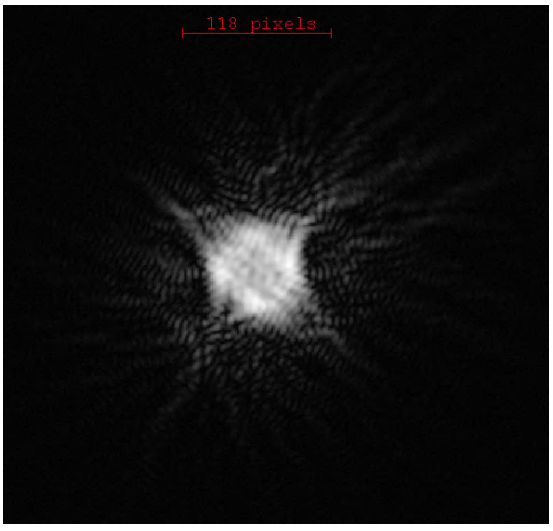

(b) PSF

Figure 5.11: Interferogram of the oblique astigmatism and its PSF

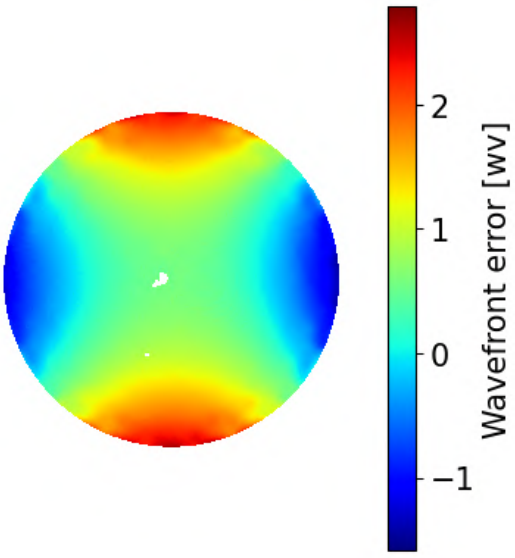

(a) Vert. astig. = -0.788 wv

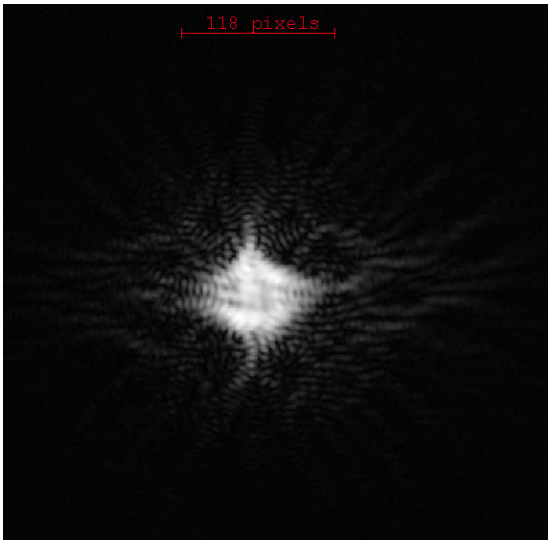

(b) PSF

Figure 5.12: Interferogram of the vertical astigmatism and its PSF

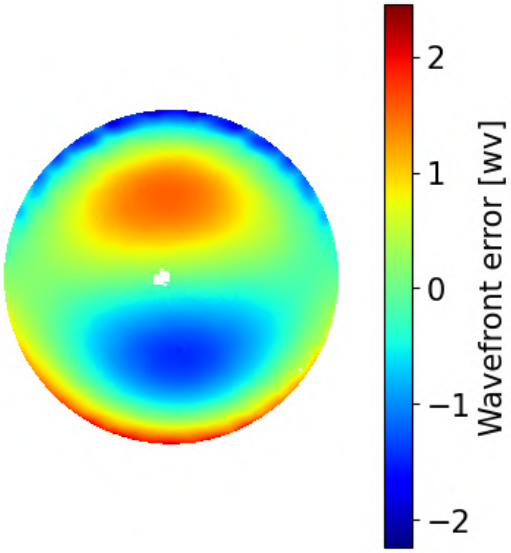

(a) Vert. coma = 0.788 wv

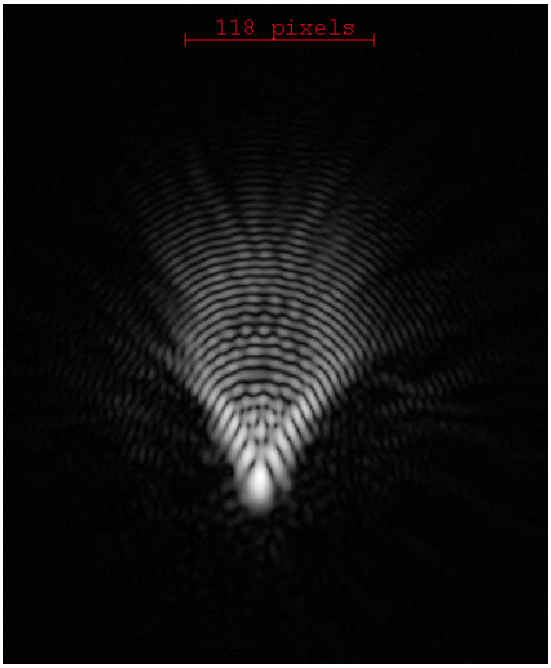

(b) PSF

Figure 5.13: Interferogram of the vertical coma and its PSF

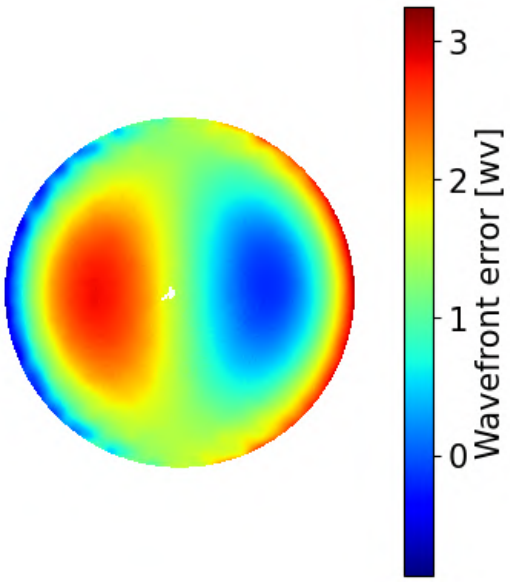

(a) Horiz. coma = 0.781 wv

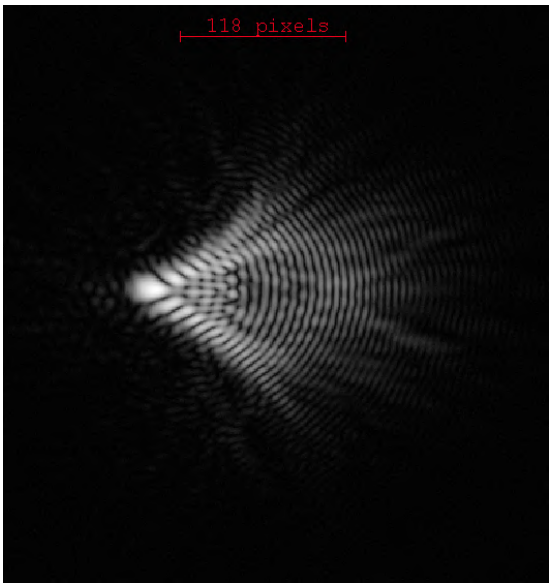

(b) PSF

Figure 5.14: Interferogram of the horizontal coma and its PSF

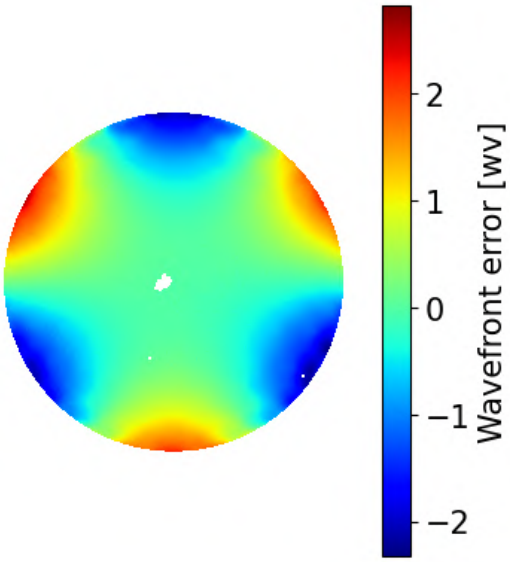

(a) Vert. tref. = -0.788 wv

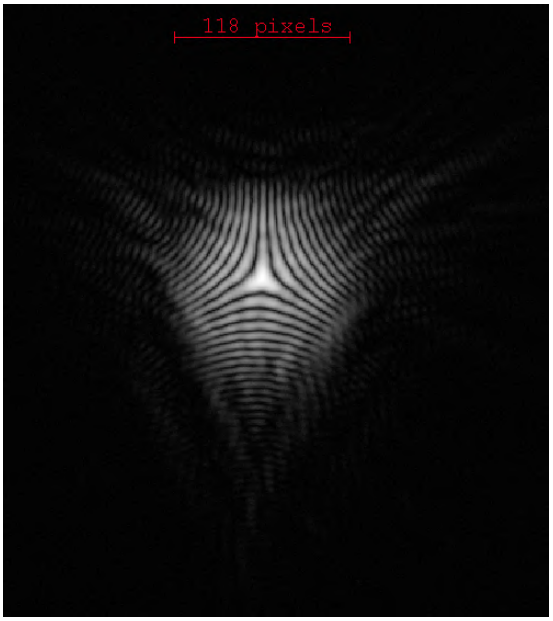

(b) PSF

Figure 5.15: Interferogram of the vertical trefoil and its PSF

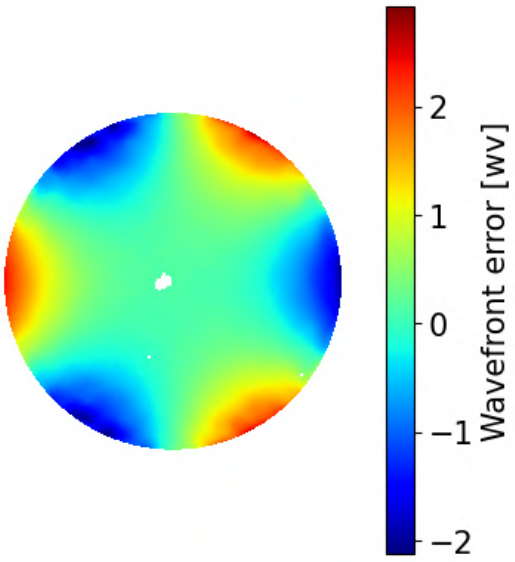

(a) Obl. tref. = -0.792 wv

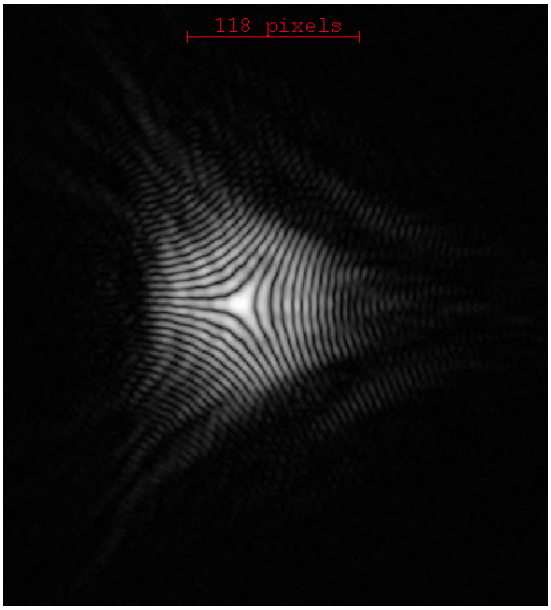

(b) PSF

Figure 5.16: Interferogram of the oblique trefoil and its PSF

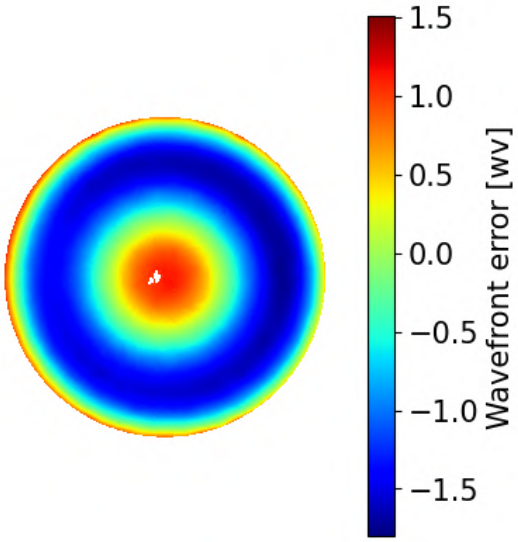

(a) Prim. sph. = 0.786 wv

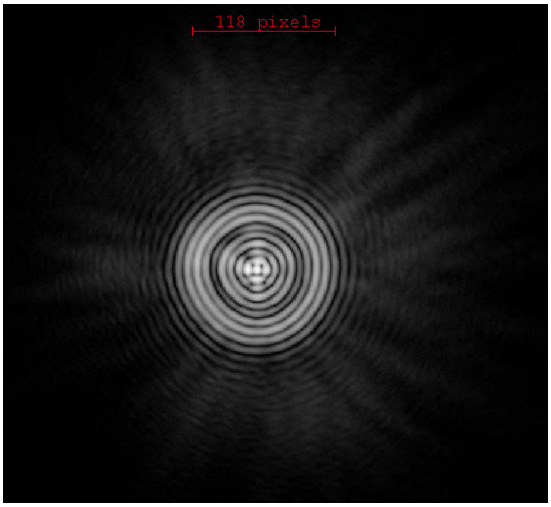

(b) PSF

Figure 5.17: Interferogram of the primary spherical and its PSF

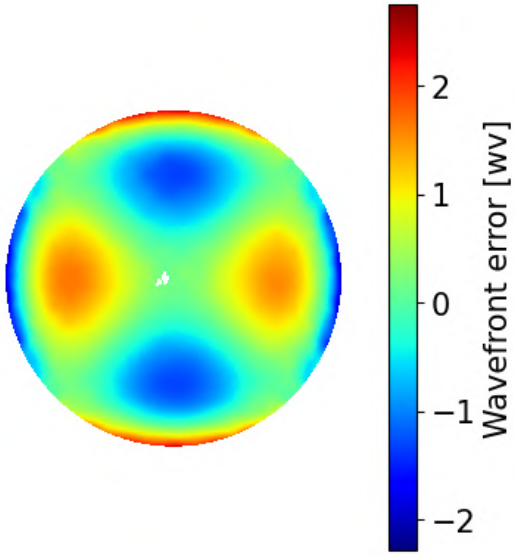

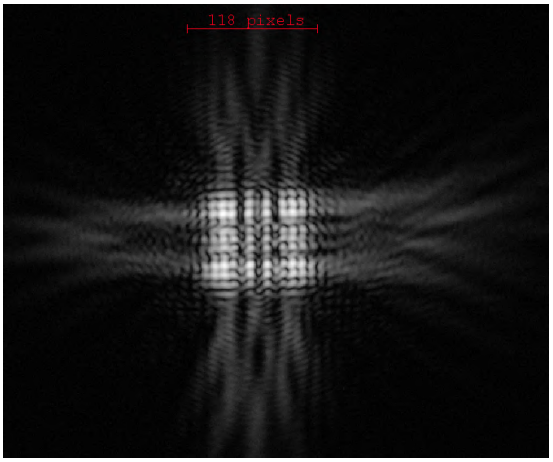

(b) PSF

(a) Vert. sec. astig. = -0.783 wv

Figure 5.18: Interferogram of the vertical secondary astigmatism and its PSF

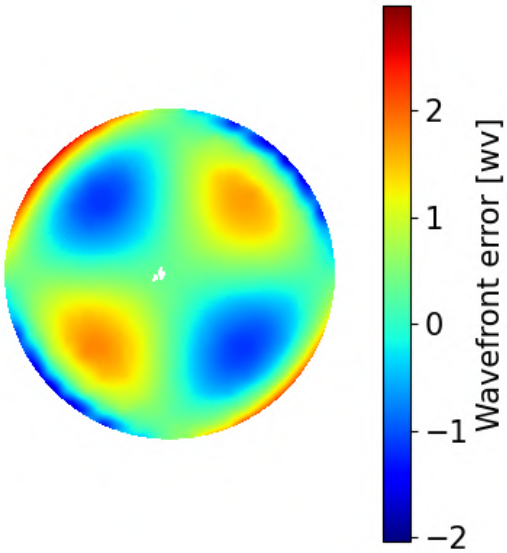

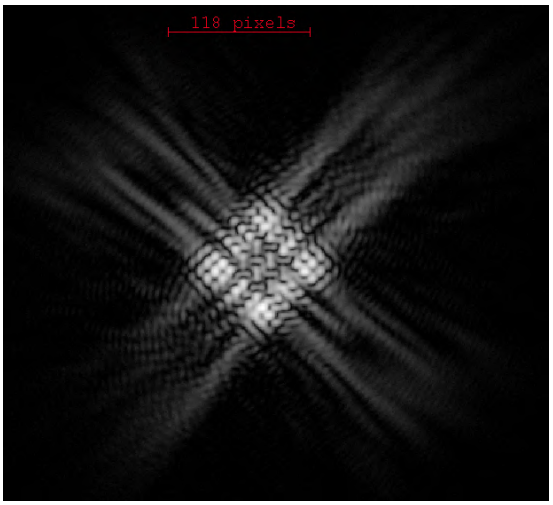

(b) PSF

(a) Obl. sec. astig. = 0.772 wv

Figure 5.19: Interferogram of the oblique secondary astigmatism and its PSF

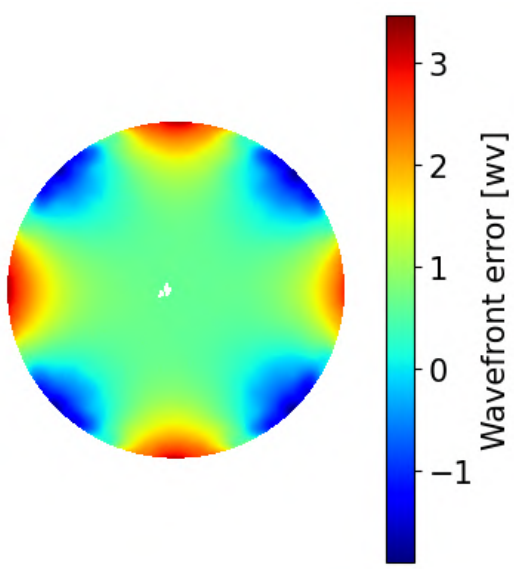

(a) Vert. quad. = 0.780 wv

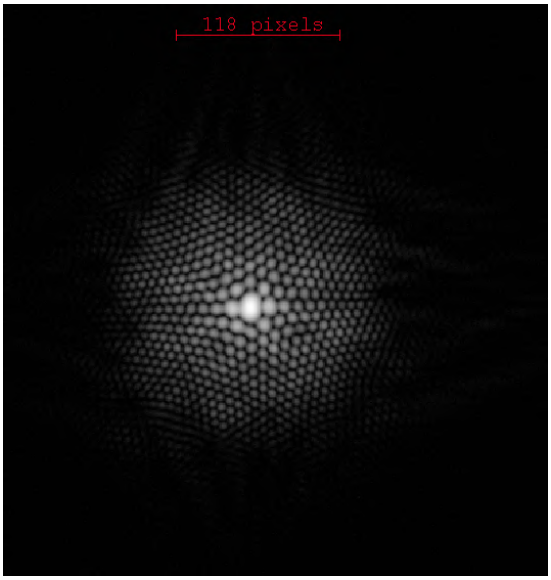

(b) PSF

Figure 5.20: Interferogram of the vertical quadrafoil and its PSF

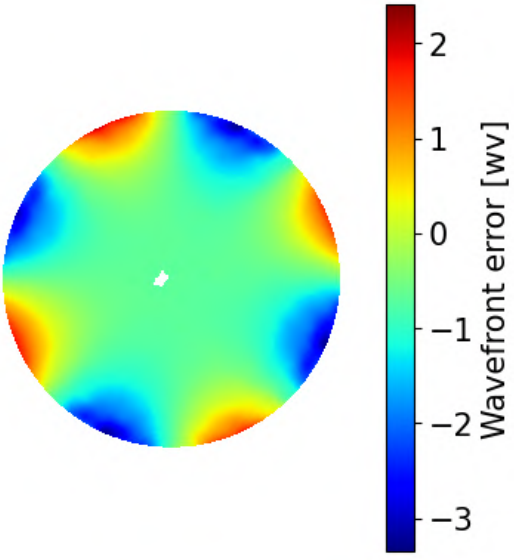

(a) Obl. quad. = -0.778 wv

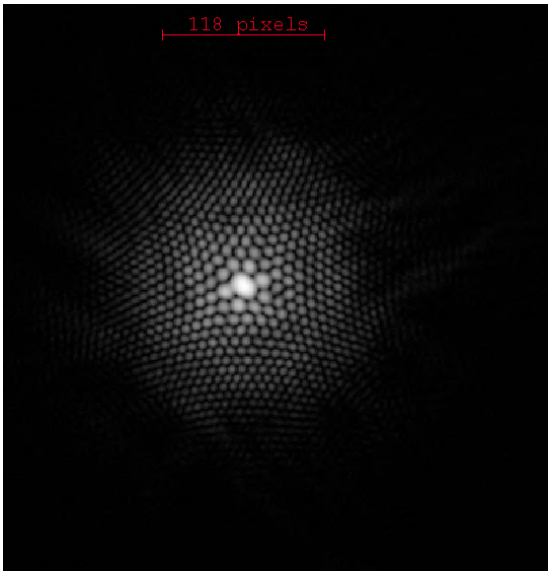

(b) PSF

Figure 5.21: Interferogram of the oblique quadrafoil and its PSF

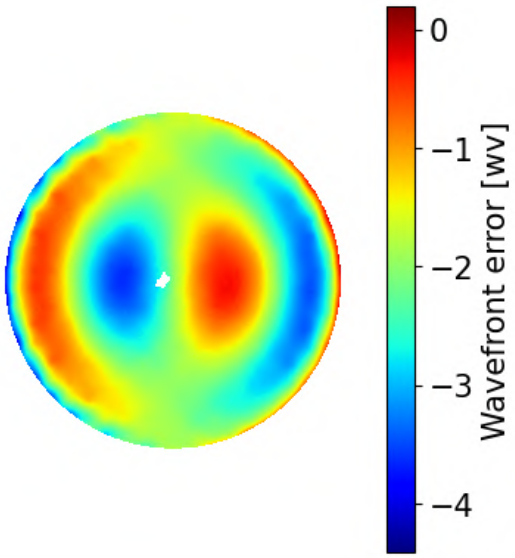

(a) Vert. sec. coma = 0.768 wv

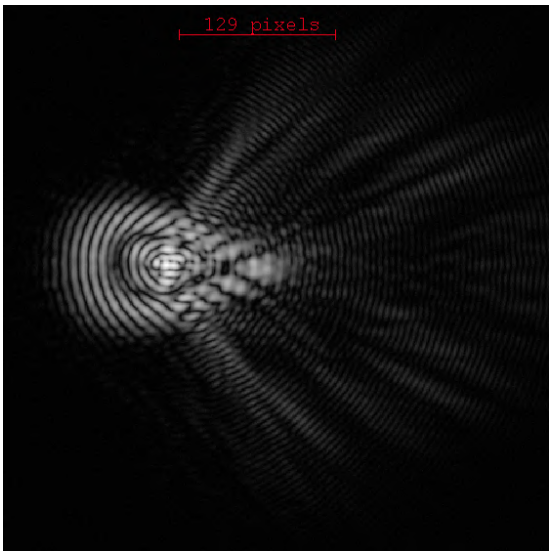

(b) PSF

Figure 5.22: Interferogram of the horizontal secondary coma and its PSF

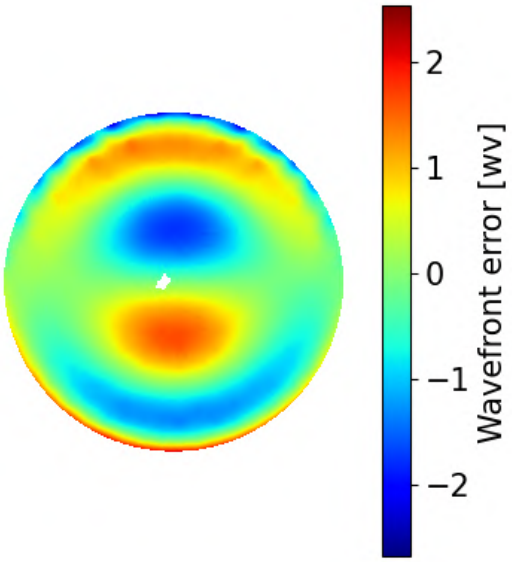

(a) Horiz. sec. coma = 0.770 wv

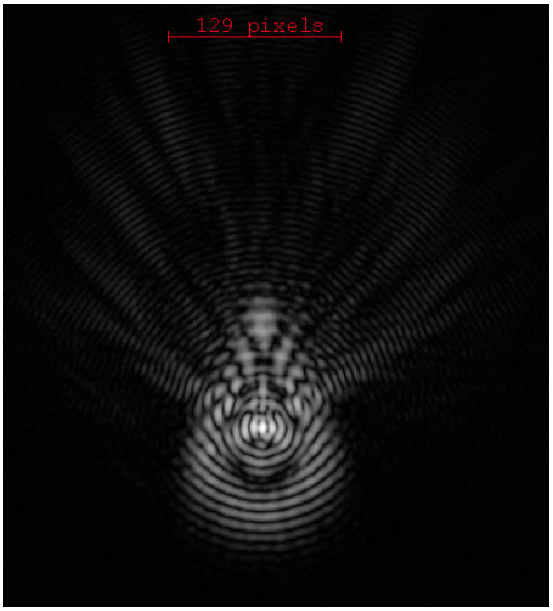

(b) PSF

Figure 5.23: Interferogram of the vertical secondary coma and its PSF

5.5 Loss of resolution on a binary system per Rayleigh criterion

At the end, I simulated a binary system affected by aberrations: this was done to prove that if a telescope performance is altered by intrinsic or exterior aberrations caused by the design or factors like the atmosphere, a DM can correct those. As much as aberrations can be introduced through a DM which lead to a loss of angular resolution, a DM can be controlled to perform the opposite operation and eliminate them. This can lead to amazingly good results for real observations, such as those shown in Fig. 5.24a from the IW tau binary system captured by the the Californian Hale telescope or the one in Fig. 5.24b of the binary system HR1852 collected by the Japanese Subaru telescope.

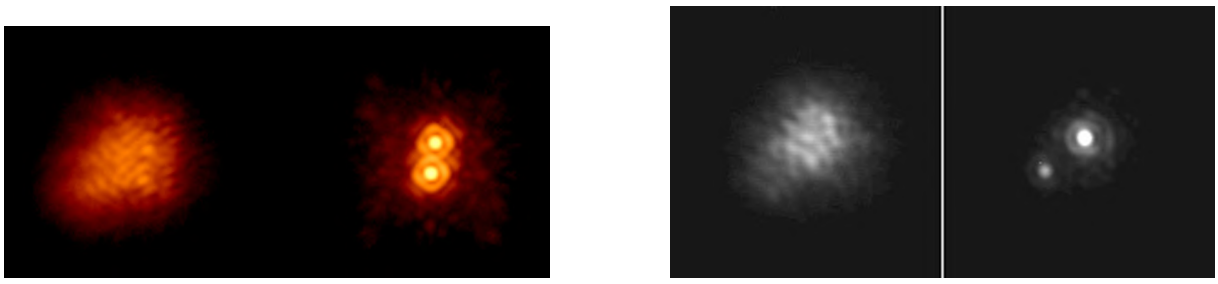

(a) (b)

Figure 5.24: On the left, the IW tau binary system corrected by the AO module of the Californian Hale telescope (credit Vik Dhillon) and, on the right, the HR1852 binary system corrected by the AO module of Japanese Subaru telescope (credit subarutelescope.org)

To achieve this objective, I set on the DM the primary aberrations that are present during observations like the tilt, defocus, astigmatism, coma, and trefoil[15]; this meant, at the end, that if I could artificially inject a certain aberration by shaping the DM, I could also correct it in the same way, in the hypothetical telescope. After selecting a mode, I recreated a binary system by adding, to the aberrated PSF, its duplicate shifted by 1 λ/D; then, I increased the amplitude until the resolution was lost per Rayleigh criterion. The results can be seen in Fig. 5.25, 5.26 and 5.27.

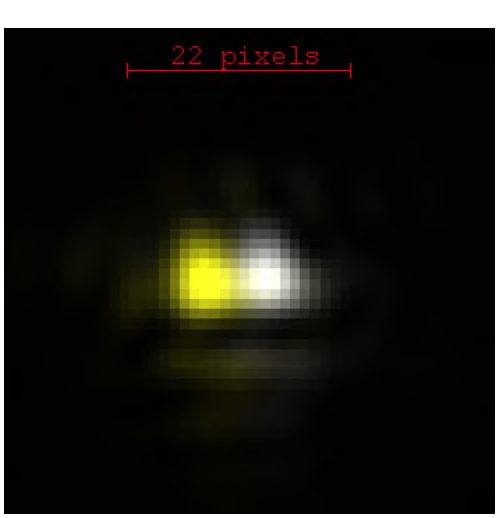

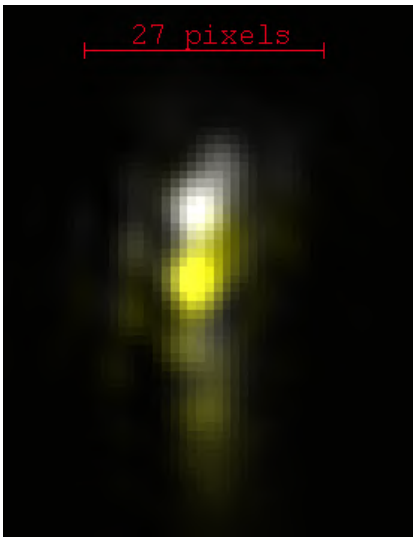

Figure 5.25: Simulated binary system affected by tilt x = 0.363 wv (left) and defocus = 0.202 wv (right)

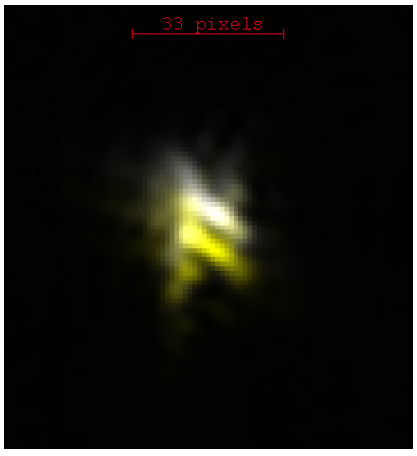

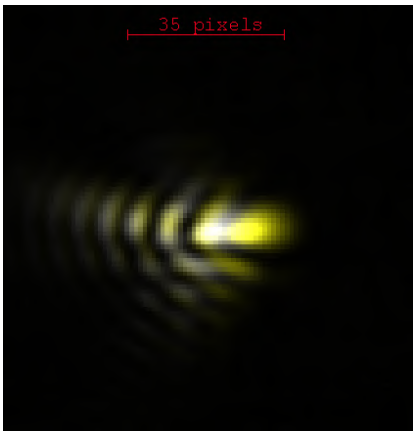

Figure 5.26: Simulated binary system affected by oblique astigmatism = 0.184 wv (left) and horizontal coma = 0.197 wv (right)

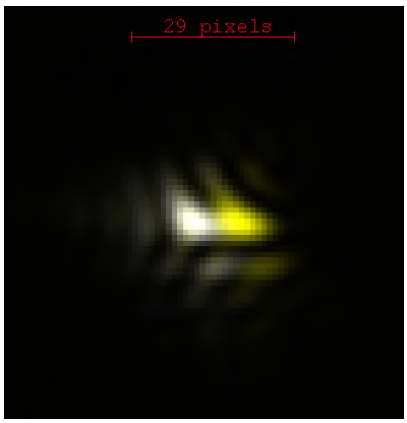

Figure 5.27: Simulated binary system affected by oblique trefoil = -0.071 wv

6

Conclusion

In modern astronomy, adaptive optics is crucial on ground-based telescopes, to reach angular resolutions that are close to ideal. As I discussed in Ch. 2, the main cause of resolution degradation is the presence of turbulence in the atmosphere: this was analyzed through the introduction of the atmospheric seeing and the parameters that describe it, like the Fried parameter, the coherence time, the Strehl ratio and the isoplanatic angle.

My thesis work was based on the characterization and control of a deformable mirror, which is one of the most important components of an adaptive optics system. As also explained in Ch. 2, nowadays AO consists of different techniques, that depend on different scientific goals, like the single and multi conjugate, the multi object and extreme adaptive optics. Nonetheless, all these are based on the so-called "closed loop" between wavefront sensing, wavefront correction through a DM and data processing.

As presented in Ch. 3, in order to correct a wavefront, a proper mathematical description of its decomposition is needed. I hence showed that the orthogonal Zernike polynomial base is particularly suitable.

In Ch. 4 and 5, I presented the work that I performed in the laboratory from the two test bench setups to the characterization of the deformable mirror.

In Ch. 4, since I needed to analyze the whole surface of the mirror using a laser interferometer, which did not cover it entirely, I described how I designed and constructed a beam expander. This proved to be the core of all the obstacles encountered: the high spherical aberration and back reflections introduced by the first singlet lens, in the first setup, were corrected by the second setup where the thermal expansion of the lenses frames became problematic on the stability of the aberrations introduced.

While taking into account the instability of the BE, in Ch. 5 I discussed how I characterized the DM: from failed tests, like the first influence function calculated which gave a

non-accurate response of the DM or the first flat which resulted in an higher than expected RMS, to the final outcome in terms of a second influence function, a best flat shape and the expected results of linear response of the actuators stroke.

The main result of my work was hence a full control of the ALPAO DM292. This meant being able to set it to any desired shape. On one hand, I could reach a flat shape with the impressive accuracy of $\lambda/43$, on the other, I could introduce any aberration of my choice. I used this last capability to present the first 17 aberrations shown as the wavefront reflected by the mirror and their respective PSF and how low-amplitude aberrations result in the loss of resolution per Rayleigh criterion in a simulated binary system. At the end, this proved that the DM292 could be used in an AO system to correct a distorted wavefront.

Due to time limitations, some tests were thought but never run, like using the Kolmogorov spectrum of a known telescope to reproduce and compare its PSF or checking the results of Ch. 5.5 using other quantitative indicators, e.g. the encircled energy. In the future, further improvements could be implemented to solve the problems introduced by the beam expander, for example using "fixable" frames which lock in place and do not experience thermal expansion or writing software routines that allow to remotely control and automatize an interferometer that has a beam diameter large enough to cover the entire mirror, i.e. a Zygo interferometer.

Bibliography

[1] Claire E. Max. Adaptive Optics: An Introduction. 2012. URL https://api.semanticscholar.org/CorpusID:124096215.

[2] John W. Hardy. *Adaptive Optics for Astronomical Telescopes*. 1998.

[3] P. Y. Madec. Overview of deformable mirror technologies for adaptive optics and astronomy. In Brent L. Ellerbroek, Enrico Marchetti, and Jean-Pierre Véran, editors, *Adaptive Optics Systems III*, volume 8447 of *Society of Photo-Optical Instrumentation Engineers (SPIE) Conference Series*, page 844705, July 2012. doi: 10.1117/12.924892.

[4] P. Krishna and Karuna Dasari. Aberrations in Theories of Optical Aberrations. *IOSR Journal of Applied Physics*, 09:37–43, 07 2017. doi: 10.9790/4861-0904013743.

[5] Roberto Ragazzoni. A package of Shack-Hartmann data reduction under IDL enviroment. *TELESCOPIO NAZIONALE GALILEO, TECHNICAL REPORT NO. 10*, February 1992.

[6] W. Boschin. TNG publications 1989-2005, 2006.

[7] G. B. Airy. On the Diffraction of an Object-glass with Circular Aperture. *Transactions of the Cambridge Philosophical Society*, 5:283, January 1835.

[8] A. Kolmogorov. The Local Structure of Turbulence in Incompressible Viscous Fluid for Very Large Reynolds' Numbers. *Akademiia Nauk SSSR Doklady*, 30:301–305, January 1941.

[9] Maria Coronel, Rodrigo Carvajal, Pedro Escárate, and Juan Aguero. Disturbance Modelling for Minimum Variance Control in Adaptive Optics Systems Using Wavefront Sensor Sampled-Data. *Sensors*, 21:3054, 04 2021. doi: 10.3390/s21093054.

[10] W.R. Hamilton. *Theory of Systems of Rays*. Number v. 1 in Nineteenth Century Collections Online (NCCO): Science, Technology, and Medicine: 1780-1925. Royal Irish Academy, 1828. URL https://books.google.it/books?id=zIV7yAEACAAJ.

[11] von F. Zernike. Beugungstheorie des schneidenver-fahrens und seiner verbesserten form, der phasenkontrastmethode. *Physica*, 1(7):689–704, May 1934. doi: 10.1016/S0031-8914(34)80259-5.

[12] R. J. Noll. Zernike polynomials and atmospheric turbulence. *Journal of the Optical Society of America (1917-1983)*, 66:207–211, March 1976.

[13] Guang ming Dai. Modal wave-front reconstruction with Zernike polynomials and Karhunen–Loève functions. *J. Opt. Soc. Am. A*, 13(6):1218–1225, Jun 1996. doi: 10.1364/JOSAA.13.001218. URL https://opg.optica.org/josaa/abstract.cfm?URI=josaa-13-6-1218.

[14] Runa Briguglio, Fernando Quirós-Pacheco, Jared R. Males, Marco Xompero, Armando Riccardi, Laird M. Close, Katie M. Morzinski, Simone Esposito, Enrico Pinna, Alfio Puglisi, Lauren Schatz, and Kelsey Miller. Optical calibration and performance of the adaptive secondary mirror at the Magellan telescope. *Scientific Reports*, 8:10835, July 2018. doi: 10.1038/s41598-018-29171-6.

[15] J. M. Hill, R. Ragazzoni, A. Baruffolo, C. J. Biddick, O. P. Kuhn, E. Diolaiti, D. Thompson, and A. Rakich. Prime focus active optics with the Large Binocular Telescope. In Larry M. Stepp and Roberto Gilmozzi, editors, *Ground-based and Airborne Telescopes II*, volume 7012 of *Society of Photo-Optical Instrumentation Engineers (SPIE) Conference Series*, page 70121M, July 2008. doi: 10.1117/12.789993.